INTEGRATED APPROACH TO FREE SPACE OPTICAL COMMUNICATIONS IN STRONG TURBULENCE

DISSERTATION

Jason A. Tellez, Lieutenant Colonel, USAF

AFIT/DEE/ENG/11-11

DEPARTMENT OF THE AIR FORCE
AIR UNIVERSITY

AIR FORCE INSTITUTE OF TECHNOLOGY

Wright-Patterson Air Force Base, Ohio

AFIT/DEE/ENG/11-11

INTEGRATED APPROACH TO FREE SPACE OPTICAL COMMUNICATIONS

IN STRONG TURBULENCE

DISSERTATION

Presented to the Faculty

Graduate School of Engineering and Management

Air Force Institute of Technology

Air University

Air Education and Training Command

in Partial Fulfillment of the Requirements for the

Degree of Doctor of Philosophy

Jason A. Tellez, B.S., M.S.
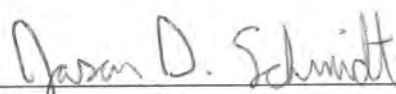
Lieutenant Colonel, USAF

September 2011

APPROVED FOR PUBLIC RELEASE; DISTRIBUTION UNLIMITED

AFIT/DEE/ENG/11-11

INTEGRATED APPROACH TO FREE SPACE OPTICAL COMMUNICATIONS

IN STRONG TURBULENCE

Jason A. Tellez, B.S., M.S.
Lieutenant Colonel, USAF
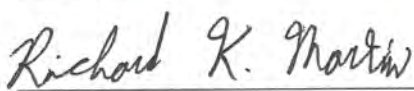
Approved:

_____   30 Aug 2011
Maj Jason D. Schmidt, PhD   Date
Chairman

_____   30 Aug 2011
Dr. Michael A. Temple   Date
Member

_____   30 Aug 2011
Dr. Richard K. Martin   Date
Member

_____   30 Aug 2011
Dr. Matthew C. Fickus   Date
Member

Accepted:

_____   _____
M. U. Thomas   Date
Dean, Graduate School of Engineering
   and Management

AFIT/DEE/ENG/11-11

Abstract

Free space optical communication (FSOC) can provide the modern warfighter
with timely, detailed information faster and more securely than traditional radio-
frequency (RF) communications systems. However, FSOC systems are vulnerable to
unique environmental factors and design constraints.

The propagation of an FSOC signal through atmospheric turbulence experiences
random fluctuations in intensity, including signal fades which negatively impact the
communications link performance. This research develops an analytical probability
density function (PDF) to model the best case scenario of using multiple independent
beams to reduce the intensity fluctuations. The PDF was further developed to account
for partially correlated beams, such as would be experienced by beams having finite
separation.

The PDF was validated with results obtained from digital simulations as well
as lab experiments. The research showed that as the number of transmitted beams
increases the probability of fade decreases. While fade probability is reduced by
adding more beams, using more than four transmitters does little to improve the
overall performance.

Pulse position modulation (PPM) provided significant improvement over tradi-
tional fixed threshold on/off keying (OOK) with the impact of signal fading reduced.
When integrating the use of PPM with four transmitted beams in a simulated airborne
FSOC system, the bit error rate (BER) was reduced by a factor of over 1×10^{-6} when
compared to the baseline of a fixed threshold OOK system with a single transmitted
beam.

Acknowledgements

First and foremost, I would like to thank my wife for supporting me during this enjoyable, yet very time-consuming chapter in my life. During the course of this research we added two new members to our family and she still maintained her unwavering support of the long hours sequestered from the rest of the family. I also want to thank my children for adding joy to otherwise mundane days and for always being curious.

I want to thank my advisor, Major Jason Schmidt, for giving me the support that I needed to accomplish this research. From helping to define the problem and scoping the research to providing ruthless editing he always there to make sure the work continued along the appropriate path.

I would also like to thank my other committee members Dr. Mike Temple, Dr. Richard Martin, and Dr. Matt Fickus for their review of this document as well as Dean's Representative Captain Matthew Garvin. Dr. Temple in particular as my Pro Tem Advisor helped to scope the entire PhD process. Finally, I would like to thank the PhD '11 Class. I was able to get to know many of you well, and consider you friends. Thanks for making this a good experience. I'm sure we'll cross paths again...

Jason A. Tellez

Table of Contents

List of Figures

List of Tables

List of Abbreviations

INTEGRATED APPROACH TO FREE SPACE OPTICAL COMMUNICATIONS IN STRONG TURBULENCE

I. Introduction

Digital high-speed communication is a vital component of the modern battlefield, helping to provide warfighters with timely, detailed information. The increase in the number of airborne and space-based sensors, as well as their increased resolution and hyperspectral capabilities, drives the need for an expanded wireless communication capacity. Optical frequencies have the potential of significantly higher data rates than traditional RF techniques, but optical fibers are not always practical. Free space optical communication (FSOC) systems provide the opportunity to take advantage of the higher data rates, as well as providing a lower probability of intercept, while avoiding some of the spectrum regulation issues associated with radio-frequency (RF) communication. The research objective is to further develop recent methods for mitigating atmosphere-induced signal fluctuations that reduce the performance of aerospace-based FSOC. Additionally, the research further develops methods to mitigate the effect of those fluctuations when they occur.

When laser beams are transmitted over long, turbulent paths, the variation in index of refraction along the path causes the beam to randomly wander and scintillate, resulting in the fluctuation of power at the receiver end of the propagation path. At times the fluctuations can result in signal fades, causing the received power to drop below the detection threshold, significantly increasing the number of bit errors. For certain engagement geometries, particularly long horizontal paths, traditional phase-only adaptive optics (AO) cannot adequately correct for the scintillation. Other non-

AO approaches, such as the propagation of partially coherent beams [5,65], multiple receivers [19], and polarization diversity [21] have also been suggested. Additional methods of dealing with the signal loss have included using keying schemes based on polarization, pulse positioning, or other modulation techniques [35].

The research used multiple transmitters separated such that each scintillates independently. Louthain and Schmidt showed that when two beams are separated by a distance of twice the Fresnel zone and propagated through a long horizontal path, they scintillate independently [31,33]. When the two beams arrive a detector, the effects of scintillation average out, reducing the probability of signal fades and their duration. In the new research reported here, the effects of additional transmitters were investigated and characterized. For practical reasons, the transmitters were arranged to minimize the amount of area occupied. Additionally, to mitigate the impact of intensity fluctuations, various modulation techniques were investigated.

To demonstrate the improved performance, first an analytical model for the turbulence irradiance fluctuations from multiple independent beams was developed. Building upon that, a model for multiple partially correlated beams was developed. This model was then combined with bit error rate (BER) models to predict the FSOC system performance. These models were then compared against results obtained from digital simulation. Finally, the model was compared with results obtained from a lab experiment simulating a FSOC system engagement.

Key contributions of this research include:

- An analytical model for the probability distribution of integrated irradiance from the propagation of multiple Gaussian beams through a turbulent atmosphere

- Demonstration of improved FSOC system performance when multiple illuminators are combined with an appropriate modulation scheme

2

- Demonstration of decreased integrated irradiance variance for multiple illuminators using experimental results, verifying the analytical model.

II. Background

This research builds upon previous research and uses principles from several disciplines, including digital communications, optical propagation, and atmospheric turbulence. This chapter reviews the relevant topics in each area with application to FSOC.

2.1 Digital communications

A model of a basic digital communications system is shown in Fig. 1. The communication of a digital bit pattern generally begins with a modulator. The modulator converts some number of bits from the input data sequence b_i into a physically measurable real-world symbol $s_i(t)$. The symbols propagate through the transmission channel and experience the channel effects which typically include AWGN. In the case of FSOC, channel effects also includes scattering, absorption, and the effects of atmospheric turbulence. The noise added within the receiver is also included in the final signal $r(t)$. From the received signal, a demodulator generates a bit estimate $\hat{b}_i$ that is passed up to the next layer, where error checking can occur.

The simplest FSOC modulation scheme is the simple on/off keying (OOK) technique where the laser is on (signal high) to transmit a symbol corresponding to a '1' and off (signal low) to transmit a symbol corresponding to a '0'. There are then four possible scenarios for a laser receiver: (1) a signal high was sent but a signal low was
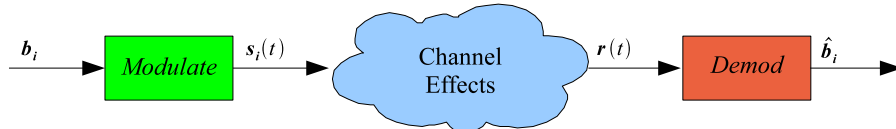
Figure 1. Block diagram of the physical layer.

estimated, (2) a signal high was sent and a signal high was estimated, (3) a signal low was sent and a signal low was estimated, and (4) a signal low was sent but a signal high was estimated. Scenarios (1) and (4) result in bit errors. The BER is typically used in communications systems to describe system performance, with the minimization of BER being the goal. The optical receiver's output voltage $r(t)$ is modeled by

$$r(t) = I(t) h(t) G + n(t),\tag{1}$$

where $I(t)$ is the transmitted irradiance pattern containing the communication signal as a function of time, $h(t)$ is the channel gain as a function of time, G is the detector conversion gain, and $n(t)$ is the additive noise as a function of time. The channel gain $h(t)$ is a random process due to the atmospheric turbulence. The additive noise $n(t)$ contains the aggregate effects of shot noise, background, and receiver electronics which together are modelled as AWGN. The receiver output is multiplied by a reference signal and integrated over the duration of symbol to generate a test statistic such that

$$z = \int_0^T s_{ref}(t) r(t) \, \mathrm{d}t,\tag{2}$$

where z is the resulting test statistic in units of Volts^2 and $s_{ref}(t)$ is the reference signal. For OOK the reference signal is simply a constant value over the symbol duration.

A maximum likelihood estimator establishes a threshold based on the test statistic probability density functions for the transmission of a '1' $p(z|H_1)$ and the transmission

of a '0' $p(z|H_0)$. The ratio test is then

$$\Lambda(z) = \frac{p(z|H_1)}{p(z|H_0)} \overset{H_1}{\underset{H_0}{\lessgtr}} \frac{p(H_0)}{p(H_1)} \qquad (3)$$

which is used to determined the most likely symbol sent. Since in most cases the probability of a '1' or '0' is equal $p(H_0) = p(H_1)$ then the equation simplifies to

$$\text{if} \quad p(z|H_1) > p(z|H_0) \quad \text{pick} \quad H_1, \qquad (4)$$

or

$$\text{if} \quad p(z|H_0) > p(z|H_1) \quad \text{pick} \quad H_0. \qquad (5)$$

For binary signals the test statistic is compared with a threshold such that Eqs. (4) and (5) simplify to

$$\text{if} \quad z > z_t \quad \text{pick} \quad H_1, \qquad (6)$$

or

$$\text{if} \quad z \le z_t \quad \text{pick} \quad H_0. \qquad (7)$$

The optimal threshold for OOK is determined by

$$z_t = \frac{\mu_0\sigma_1^2 - \mu_1\sigma_0^2}{\sigma_1^2 - \sigma_0^2} + \frac{\sigma_1\sigma_0}{\sigma_1^2 - \sigma_0^2}\sqrt{(\mu_1 - \mu_0)^2 + 2(\sigma_1^2 - \sigma_0^2)\ln\left(\frac{\sigma_1}{\sigma_0}\right)}, \qquad (8)$$

where $\mu_{0,1}$ is the mean value for z for a '0' and '1' respectively and $\sigma_{0,1}$ is the variance of z associated with a '0' and '1' respectively [6, 14, 30].

2.2 Free space optical propagation

For FSOC, light is used to create the symbol, representing a bit or packet of bits, which is propagated through an open medium. Before considering the turbulent effects that the medium has on the propagated light, vacuum propagation is considered. Since most laser beams can be well-represented by Gaussian beams, the propagation of Gaussian beams is also discussed.

2.2.1 Vacuum propagation.

If a propagation medium is linear, isotropic, homogeneous, non-dispersive, and nonmagnetic, then Maxwell's equations can be reduced to the scalar wave equation

$$\nabla^2 u\left(P, t\right) - \frac{n^2}{c^2} \frac{\partial^2 U\left(P, t\right)}{\partial t^2} = 0, \tag{9}$$

where n is the index of refraction of the medium, c is the speed of light, u represents any of the scalar field components at a position P and a time t [20]. If it is further assumed that the propagated light is monochromatic then the scalar field can be described as

$$u\left(P, t\right) = A\left(P\right) \cos\left[2\pi\nu t + \phi\left(P\right)\right], \tag{10}$$

where $A\left(P\right)$ and $\phi\left(P\right)$ are the amplitude and phase of the wave at a position P, and ν is the optical frequency. More compactly, Eq. (10) becomes

$$u\left(P, t\right) = Re\left\{U\left(P\right) \exp\left(-i2\pi\nu t\right)\right\}, \tag{11}$$

where $Re\left\{\right\}$ signifies the "real part", and $U\left(P\right)$ is the complex phasor

$$U\left(P\right) = A\left(P\right) \exp\left[-i\phi\left(P\right)\right]. \tag{12}$$

Since the time dependence is always $\exp\left(-i2\pi\nu t\right)$ for a traveling wave, then U must obey the time-independent Helmholtz equation

$$\left(\nabla^2 + k^2\right) U = 0, \tag{13}$$

where $k = 2\pi/\lambda$ with λ being the field wavelength. Solving Eq. (13) using Green's theorem and the free-space Green's function provides the Huygens-Fresnel principle [20]

$$U\left(P_1\right) = \frac{1}{i\lambda} \iint\limits_{\Sigma} U\left(P_0\right) \frac{\exp\left(ik\boldsymbol{r_{01}}\right)}{\boldsymbol{r_{01}}} \cos\theta \mathrm{d}s, \tag{14}$$

where $U\left(P_0\right)$ and $U\left(P_1\right)$ are the incident and diffracted fields, θ is the angle between the aperture normal, the vector $\boldsymbol{r}_{01}$ pointing from P_0 to P_1, and Σ defines the aperture area.

The Huygens-Fresnel principle can be re-written in Cartesian coordinates as

$$U\left(x, y\right) = \frac{z}{i\lambda} \iint\limits_{\Sigma} U\left(\xi, \eta\right) \frac{\exp\left(ikr_{01}\right)}{r_{01}^2} \mathrm{d}\xi \mathrm{d}\eta, \tag{15}$$

by noting that the term $\cos\theta$ is given by

$$\cos\theta = \frac{z}{r_{01}} \tag{16}$$

and the distance r_{01} is given by

$$r_{01} = \sqrt{z^2 + \left(x - \xi\right)^2 + \left(y - \eta\right)^2}. \tag{17}$$

Approximations include scalar diffraction and that $r_{01} \gg \lambda$. Further, by taking the first two terms of the binomial expansion of Eq. (17), the resulting Fresnel diffraction

integral can be expressed as

$$U(x,y) = \frac{e^{ikz}}{i\lambda z} \int_{-\infty}^{\infty} \int_{-\infty}^{\infty} U(\xi,\eta) e^{i\frac{k}{2z}\left[(x-\xi)^2+(y-\eta)^2\right]} d\xi d\eta, \tag{18}$$

where $U(\xi,\eta)$ is the original field and $U(x,y)$ is the result of propagating a distance of z. Re-writing in terms of a Fourier transform and performing some algebra yields

$$U(x,y) = \frac{e^{ikz}}{i\lambda z} e^{i\frac{k}{2z}\left(x^2+y^2\right)} \mathcal{F}\left\{U(\xi,\eta) e^{i\frac{k}{2z}\left(\xi^2+\eta^2\right)}\right\}\Bigg|_{f_X=\frac{x}{\lambda z}, f_Y=\frac{y}{\lambda z}}. \tag{19}$$

This form shows that the propagated field is merely a scaled Fourier of the original field multiplied by a quadratic phase factor demonstrating that the Fresnel diffraction integral is useful for linear systems analysis.

2.2.2 Propagation of Gaussian beams.

Most optical beams propagating in free space can be modeled as purely transverse electro-magnetic (TEM) modes [63]. The lowest-order Gaussian beam mode, TEM_{00}, is typically used to model a laser beam, with limiting cases including plane-waves and spherical-waves. The Gaussian beam mode is found by solving the wave equation. This section describes the vacuum propagation of a TEM_{00} mode Gaussian beam.

A Gaussian laser can be parameterized by its $1/e$ radius W_0, its radius of curvature F_0, and its wavelength λ. The optical field at the source plane of the TEM_{00} wave can then be defined as [1]

$$U_0(r, z=0) = a_0 \exp\left(-\frac{r^2}{W_0^2} - \frac{ikr^2}{2F_0}\right) = a_0 \exp\left(-\frac{1}{2}\alpha_0 kr^2\right), \tag{20}$$

where $r = \left(x^2 + y^2\right)^{1/2}$ is the radial distance from the beam center, z is the propagation distance, a_0 is the optical field amplitude in $(\text{W/m}^2)^{1/2}$, and α_0 is the complex

beam parameter related to spot size and phase front radius such that

$$\alpha_0 = \frac{2}{kW_0^2} + i\frac{1}{F_0}. \tag{21}$$

The propagation beam parameter $p(z)$ is expressed in the form

$$p(z) = 1 + i\alpha_0 z = \Theta_0 + i\Lambda_0, \tag{22}$$

where Θ_0 and Λ_0 are the input beam parameters defined as the real and imaginary parts of $p(z)$ such that

$$\Theta_0 = 1 - \frac{z}{F_0}, \quad \Lambda_0 = \frac{2z}{kW_0^2}. \tag{23}$$

The parameter Θ_0 is also known as the curvature parameter while Λ_0 is the Fresnel ratio at the input plane. For a fixed path length and initial radius of curvature F_0, the curvature parameter for collimated, convergent, and divergent beams are $\Theta_0 = 1$, $\Theta_0 < 1$, and $\Theta_0 > 1$, respectively. The limiting cases of a plane-wave and spherical-wave (i.e. point source) are modeled with $W_0 = \infty$m and $W_0 = 0$m resulting in $\Lambda_0 = 0$ and $\Lambda_0 = \infty$, respectively.

The propagated Gaussian beam, determined by solving the wave equation, is

$$U_0(r, z) = \frac{1}{\sqrt{\Theta_0^2 + \Lambda_0^2}} \exp\left(-\frac{r^2}{W^2}\right) \exp\left[i\left(kz - \varphi - \frac{kr^2}{2F}\right)\right], \tag{24}$$

where φ, W, and F represent the longitudinal phase shift, spot size radius, and radius of curvature at a position z along the propagation path. These are defined in terms of the input beam parameters as

$$\varphi = \tan^{-1}\frac{\Lambda_0}{\Theta_0}, \tag{25}$$

10

$$W = W_0 \sqrt{\Theta_0^2 + \Lambda_0^2}, \tag{26}$$

$$F = \frac{F_0 \left(\Theta_0^2 + \Lambda_0^2\right)\left(\Theta_0 - 1\right)}{\Theta_0^2 + \Lambda_0^2 - \Theta_0}. \tag{27}$$

From this, the output-plane beam parameters are defined as

$$\Theta = 1 + \frac{z}{F}, \quad \Lambda = \frac{2z}{kW^2}. \tag{28}$$

2.3 Atmospheric turbulence

Atmospheric turbulence degrades the FSOC performance in several ways. The propagated beam is dispersed and moved about, limiting the amount of light incident on the receiver. Additionally, higher-order intensity fluctuations vary the amount of light incident on the receiver. Ultimately, the turbulence causes fades in the signal intensity resulting in errors in the bit estimates. Even seemingly short fades, like 1msec, for a 1Gbit/sec system could result in as many as 500,000 bit errors.

2.3.1 Atmospheric fluctuations of index of refraction.

Optical turbulence in the atmosphere results from fluctuations in the index of refraction due to turbulent air motion through the variation of the pressure, temperature, and velocity of air. Light propagating through this turbulent medium experiences distortion, both spatially and temporally, resulting in the twinkling of stars, loss of resolution for imaging systems, and the distortion of propagating laser beams.

The ultimate source of the turbulence arises from the heating and cooling of the surface of the earth caused by sunlight and the diurnal cycle, which cause large-scale variations in air temperature. Kolmogorov developed a model for the velocity structure function and power spectral density (PSD) of turbulent velocity. He suggested that the kinetic energy in large-scale motion gets transferred to smaller scale motions

resulting in a transition from turbulent to laminar flow [47]. This allowed others to apply similar analysis to temperature and thus derive a model of the refractive-index structure function and PSD [12, 37].

At optical wavelengths, the dependence of the index of refraction of air on temperature and pressure is

$$n = n_0 + \frac{77.6P}{T} \times 10^{-6},$$ (29)

where $n_0 = 1$, T is the air temperature in Kelvins, and P is the air pressure in millibars. The temperature fluctuations normally dominate the index of refraction variations. However, in boundary layer regions, such as around an optical window on an airframe, the pressure variations can be large enough to cause significant changes in the index of refraction.

The statistical distribution of the size and number of the turbulence eddies, regions of uniform index of refraction, is characterized by the power spectral density of $n(\boldsymbol{r})$, denoted by

$$\Phi_n(\boldsymbol{\kappa}) = \left(\frac{1}{2\pi}\right)^3 \int_{-\infty}^{\infty} B_n(\boldsymbol{r}) \exp(-i\boldsymbol{\kappa} \cdot \boldsymbol{r}) \, \mathrm{d}\boldsymbol{r},$$ (30)

where $B_n(\boldsymbol{r})$ is the autocorrelation of $n(\boldsymbol{r})$ and $\boldsymbol{r}$ is a position vector. The independent variable $\boldsymbol{\kappa}$ is the spatial wavenumber vector with orthogonal components along the x, y, and z directions. Under conditions where homogeneous, isotropic turbulence is assumed, the power spectral density of the index of refraction fluctuations is a function of the scalar wavenumber

$$\kappa = \sqrt{\kappa_x^2 + \kappa_y^2 + \kappa_z^2},$$ (31)

which is related to the isotropic scale size by $l = 2\pi/\kappa$.

Standard Kolmogorov theory does not predict a mathematical form for $\Phi_n(\boldsymbol{\kappa})$ outside of the region where larger eddies break up into smaller ones. The quantity L_0

is referred to as the outer scale and l_0 the inner scale, between which this assumption holds true. When κ is within the range $2\pi/L_0 \ll \kappa \ll 2\pi/l_0$, the form of $\Phi_n(\boldsymbol{\kappa})$ predicted by Kolmogorov theory is [47]

$$\Phi_n^K(\boldsymbol{\kappa}) = 0.033 C_n^2 \kappa^{-11/3}, \tag{32}$$

where C_n^2 is the index of refraction structure constant with units of $\text{m}^{-2/3}$ and the superscript K is used to denote the Kolmogorov spectrum. When inner and outer scales are considered, when operating outside the range where $2\pi/L_0 \ll \kappa \ll 2\pi/l_0$, the modified von Kármán spectrum model is used and is represented by [47]

$$\Phi_n^V(\boldsymbol{\kappa}) = \frac{0.033 C_n^2}{\left(\kappa^2 + \kappa_0^2\right)^{11/6}} \exp\left(-\frac{\kappa^2}{\kappa_m^2}\right), \tag{33}$$

where $\kappa_0 = 2\pi/L_0$, $\kappa_m = 5.92/l_0$, and the superscript V denotes the von Kármán spectrum.

For most problems of interest, the atmospheric turbulence strength varies along the propagation path. In this case, the index of refraction structure parameter becomes $C_n^2(z)$ where z is longitudinal position along the path. Using this notation, the Kolmogorov and von Kármán spectrums from Eqs. (32) and (33) become

$$\Phi_n^K(\boldsymbol{\kappa}, z) = 0.033 C_n^2(z) \kappa^{-11/3}, \tag{34}$$

and

$$\Phi_n^V(\boldsymbol{\kappa}, z) = \frac{0.033 C_n^2(z)}{\left(\kappa^2 + \kappa_0^2\right)^{11/6}} \exp\left(-\frac{\kappa^2}{\kappa_m^2}\right), \tag{35}$$

respectively.

A commonly used model of C_n^2 is the Hufnagel-Valley turbulence profile described
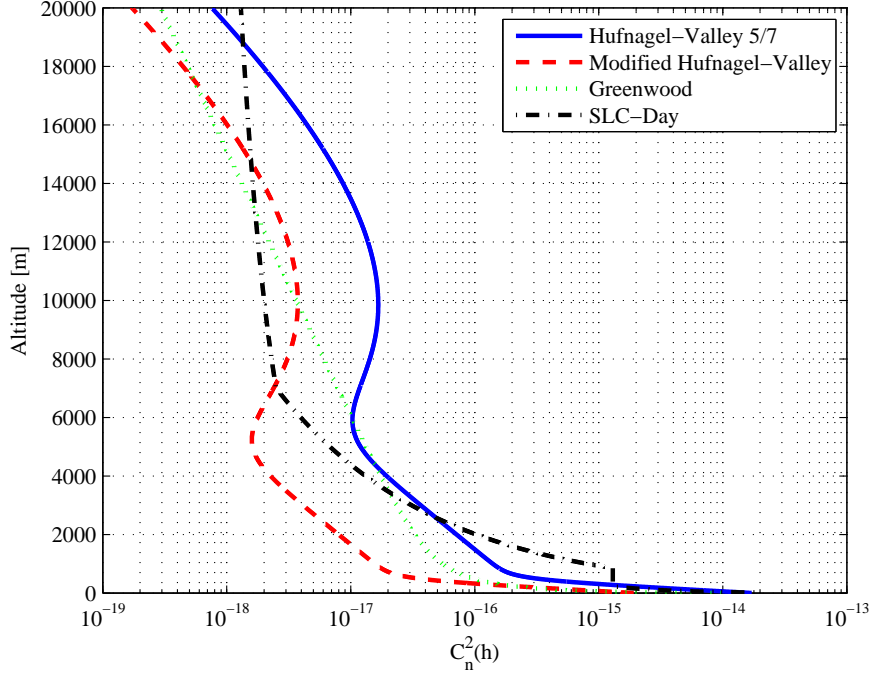
Figure 2. Comparison of C_n^2 profiles.

by [47]

$$C_n^2(h) = 5.94 \times 10^{-53} (v/27)^2 h^{10} \exp\left(-\frac{h}{1000}\right)$$
$$+ 2.7 \times 10^{-16} \exp\left(-\frac{h}{1500}\right) + A \exp\left(-\frac{h}{100}\right), \quad (36)$$

where h is the height above the ground in meters, A is a free parameter that sets the turbulence strength near the ground with units of $m^{-2/3}$, and v is a free parameter that sets the high-altitude wind speed with units of m/s. Commonly used values are $A = 1.7 \times 10^{-14} m^{-2/3}$ and $v = 21$m/s, often referred to as the $HV_{5/7}$ model. Other models include the SLC-Day model, the Modified Hufnagel-Valley model, and the Greenwood model. A comparison between the models is shown in Fig. 2.

14

2.3.2 Atmospheric turbulence parameters.

The effects of atmospheric turbulence are observed through several optical phenomena. These include phase and amplitude effects, which cause laser beams to spread, wander, and scintillate. The quantities used to describe the accumulated phase effects include the atmospheric coherence length and the isoplanatic angle, while quantities describing the amplitude effects include log-amplitude variance and intensity variance.

The development of the phase and amplitude effects starts with the stochastic Helmholtz equation

$$\nabla^2 U + k^2 n^2 \left(\boldsymbol{r} \right) U = 0, \tag{37}$$

where the refractive index is expressed as a function of position $\boldsymbol{r}$

$$n \left(\boldsymbol{r} \right) = n_0 + n_1 \left(\boldsymbol{r} \right), \tag{38}$$

and $n_0 = \langle n \left(\boldsymbol{r} \right) \rangle \cong 1$. Using the Rytov method, one of several methods to solve for the turbulence effects, the field of the electromagnetic wave is written as

$$U \left(\boldsymbol{R} \right) \equiv U \left(\boldsymbol{r}, L \right) = U_0 \left(\boldsymbol{r}, L \right) \exp \left[\psi \left(\boldsymbol{r}, L \right) \right]. \tag{39}$$

The complex phase perturbation due to the turbulence, ψ, is of the form

$$\psi \left(\boldsymbol{r}, L \right) = \psi_1 \left(\boldsymbol{r}, L \right) + \psi_2 \left(\boldsymbol{r}, L \right) + \cdots, \tag{40}$$

where $\psi_1 \left(\boldsymbol{r}, L \right)$ and $\psi_2 \left(\boldsymbol{r}, L \right)$ represent the first-order and second-order perturbations, respectively. Various statistical moments of the perturbations can then be computed,

for example

$$E_1(0,0) = \langle \psi_2(\boldsymbol{r}, L) \rangle + \frac{1}{2} \langle \psi_1^2(\boldsymbol{r}, L) \rangle \tag{41}$$

$$= -2\pi^2 k^2 \int_0^L \int_0^\infty \kappa \Phi_n(\boldsymbol{\kappa}, z) \, \mathrm{d}\kappa \mathrm{d}z, \tag{42}$$

where then the appropriate spectrum (Kolmogorov, von Kármán, etc.) could be used. This moment and others then can provide the basis for parameters used to describe the phase and amplitude effects of propagation through turbulence.

The effect of beam spreading is related to the limiting effect of the atmosphere on imaging resolution. Without atmospheric turbulence, the resolution of an imaging system is determined by the aperture diameter, known as the diffraction limit. When atmospheric turbulence is considered, imaging system resolution can be approximated by replacing the aperture diameter with the atmospheric coherence diameter r_0 also known as the Fried parameter [16]. Using the Kolmogorov spectrum, for a plane-wave, this results in [49]

$$r_{0,pw} = \left[0.423 k^2 \int_0^L C_n^2(z) \, \mathrm{d}z \right]^{-3/5} \tag{43}$$

and for a spherical-wave the result is

$$r_{0,sw} = \left[0.423 k^2 \int_0^L C_n^2(z) \left(\frac{z}{L} \right)^{5/3} \mathrm{d}z \right]^{-3/5}, \tag{44}$$

where $k = 2\pi/\lambda$ is the wavenumber and L is the propagation path length. The plane-wave and spherical-wave results provide limiting cases for a Gaussian beam. Therefore, it is common to use the Gaussian beam parameters to determine whether it behaves more like a planar or spherical-wave and then use the corresponding equation.

Compensation for the phase distortions in the atmosphere relies upon an idealized point source beacon in the vicinity of the object to be observed. How close this point

16

source needs to be is determined by the turbulence along the path. The separation is given as the isoplanatic angle and is found via [49]

$$\theta_0 = \left[2.91 k^2 \int_0^L C_n^2 (z) (L - z)^{5/3} \, \mathrm{d}z \right]^{-3/5}. \tag{45}$$

As long as the reference and the object to be observed are within this angular extent, phase compensation based on the reference can effectively compensate for the distortions that the image experiences.

Atmospheric distortion of a laser beam also includes amplitude effects, also known as scintillation. As the beam propagates through the atmosphere, the cumulative effects of phase aberrations result in constructive and destructive interference at the receiver, which are observed as intensity variations. For laser communications systems, these effects are particularly important since they can cause signal fades resulting in bit errors. This phenomenon can be characterized by the log-amplitude variance σ_χ^2, commonly referred to as the Rytov number $\mathcal{R}$ and is calculated using the Rytov approximation. Turbulence strength is often expressed in terms of the Rytov number. The plane-wave log-amplitude variance at the receiver is [1]

$$\sigma_{\chi,pw}^2 = 0.5631 k^{7/6} \int_0^L C_n^2 (z) (L - z)^{5/6} \, \mathrm{d}z, \tag{46}$$

and the spherical-wave log-amplitude variance is

$$\sigma_{\chi,pw}^2 = 0.5631 k^{7/6} \int_0^L C_n^2 (z) \left(\frac{z}{L} \right)^{5/6} (L - z)^{5/6} \, \mathrm{d}z. \tag{47}$$

The expressions in Eqs. (46) and (47) are only valid for weak turbulence, where the log-amplitude variances is $\sigma_\chi^2 < 0.25$. For moderate to strong turbulence, when $\sigma_\chi^2 > 0.25$, the scintillation begins to saturate and the Rytov approximation no longer

holds. For horizontal propagation (i.e, constant turbulence) of plane-waves, the log-amplitude variance reduces to

$$\sigma_{\chi,pw}^2 = 0.3071 k^{7/6} C_n^2 L^{11/6}. \tag{48}$$

The detector at the receiver measures irradiance, not the field amplitude directly. For weak turbulence, the normalized irradiance variance (also known as the scintillation index) σ_I^2 is [1]

$$
\begin{aligned}
\sigma_{\frac{I}{\langle I \rangle}}^2 (r) &= \frac{\langle I^2 (r) \rangle}{\langle I (r) \rangle^2} - \frac{\langle I (r) \rangle^2}{\langle I (r) \rangle^2} = \frac{\langle I^2 (r) \rangle}{\langle I (r) \rangle^2} - 1 \tag{49} \\
&= \exp \left[\sigma_\chi^2 (r) \right] - 1 \tag{50} \\
&\cong 4\sigma_\chi^2 (r) \quad \text{for } \sigma_\chi^2 < 0.25 \tag{51} \\
&\cong \sigma_{\ln I}^2 (r) \quad \text{for } \sigma_\chi^2 < 0.25, \tag{52}
\end{aligned}
$$

where r is the radial distance from the optical axis and $\sigma_{\ln I}^2 (r)$ is the log-irradiance variance. Based on this relationship, the plane-wave scintillation index is

$$\sigma_{\ln I}^2 = 2.251 k^{7/6} \int_0^L C_n^2 (z) (L - z)^{5/6} \, \mathrm{d}z, \tag{53}$$

and for a spherical-wave is

$$\sigma_{\ln I}^2 = 2.251 k^{7/6} \int_0^L C_n^2 (z) \left(\frac{z}{L} \right)^{5/6} (L - z)^{5/6} \, \mathrm{d}z. \tag{54}$$

Andrews and Phillips define the plane-wave scintillation index for a constant C_n^2 profile as the Rytov variance σ_R^2, which is not to be confused with the Rytov number [1]. From Eq. (53), the Rytov variance is defined as

$$\sigma_R^2 = \sigma_1^2 = 1.23 k^{7/6} C_n^2 L^{11/6}. \tag{55}$$

18

For strong turbulence, Rytov numbers larger than 0.25, the phase variance continues to increase while the amplitude variance saturates. Several theories have been used to predict this behavior as the Rytov number increases [1]. Extended Rytov theory breaks the normalized irradiance into two factors according to

$$\hat{I} = \frac{I}{\langle I \rangle} = XY, \tag{56}$$

where $\hat{I}$ is the normalized irradiance, X arises from large-scale turbulent eddy effects, and Y arises from statistically independent small-scale turbulent eddy effects. The small-scale and large-scale variances are typically modeled as Gamma random variables, resulting in I being a Gamma-Gamma random variable. The normalized ($\langle I \rangle = 1$) Gamma-Gamma distribution's probability distribution function (PDF) is given by

$$p(I) = \frac{2(\alpha\beta)^{(\alpha+\beta)/2}}{\Gamma(\alpha)\Gamma(\beta)} I^{(\alpha+\beta)/2-1} K_{\alpha-\beta}\left(2\sqrt{\alpha\beta I}\right), \quad I > 0, \tag{57}$$

where $\alpha = 1/\sigma_x^2$, $\beta = 1/\sigma_y^2$, $\Gamma(\cdot)$ is the Gamma function and $K_p(\cdot)$ is the modified Bessel function of the second kind. More often, the cumulative distribution function (CDF) is used to determine fade statistics, since it describes the probability of receiving less than a given threshold. The CDF for the Gamma-Gamma function can be determined analytically to be

$$\begin{aligned}
P(I \leq I_T) &= \int_0^{I_T} p(I)\, dI \\
&= \frac{\pi}{\sin[\pi(\alpha-\beta)]\,\Gamma(\alpha)\,\Gamma(\beta)} \\
&\quad \times \left\{ \frac{(\alpha\beta I_T)^{\beta}}{\beta\Gamma(\beta_1)} {}_1F_2(\beta; \beta+1, \beta_1; \alpha\beta I_T) \right. \\
&\quad \left. - \frac{(\alpha\beta I_T)^{\alpha}}{\alpha\Gamma(\alpha_1)} {}_1F_2(\alpha; \alpha+1, \alpha_1; \alpha\beta I_T) \right\},
\end{aligned} \tag{58}$$

19

where I_T is a threshold, $\beta_1 = \beta - \alpha + 1$, $\alpha_1 = \alpha - \beta + 1$ and $_1F_2$ is a generalized hypergeometric function.

The total scintillation index then takes the form of

$$\sigma_I^2 = \exp\left(\sigma_{\ln I}^2\right) - 1 = \exp\left(\sigma_{\ln X}^2 + \sigma_{\ln Y}^2\right) - 1, \tag{59}$$

where $\sigma_{\ln X}^2$ and $\sigma_{\ln Y}^2$ are the variances of the small- and large-scale irradiance fluctuations, respectively. As with the equations for weak turbulence, the equations for $\sigma_{\ln X}^2$ and $\sigma_{\ln Y}^2$ take different forms depending on the type of source. For Kolmogorov turbulence (i.e, zero inner-scale and infinite outer-scale) the log variances are given by [1]

$$\sigma_{\ln X}^2 = \frac{0.49\sigma_R^2}{\left(1 + 1.11\sigma_R^{12/5}\right)^{7/6}} \approx \begin{cases} 0.49\sigma_R^2, & \sigma_R^2 \ll 1, \\ \frac{0.49}{\sigma_R^{4/5}}, & \sigma_R^2 \gg 1, \end{cases} \tag{60}$$

and

$$\sigma_{\ln Y}^2 = \frac{0.51\sigma_R^2}{\left(1 + 0.69\sigma_R^{12/5}\right)^{7/6}} \approx \begin{cases} 0.51\sigma_R^2, & \sigma_R^2 \ll 1, \\ \ln 2, & \sigma_R^2 \gg 1, \end{cases} \tag{61}$$

for a plane-wave and

$$\sigma_{\ln X}^2 = \frac{0.20\sigma_R^2}{\left(1 + 0.19\sigma_R^{12/5}\right)^{7/6}} \approx \begin{cases} 0.20\sigma_R^2, & \sigma_R^2 \ll 1, \\ \frac{1.37}{\sigma_R^{4/5}}, & \sigma_R^2 \gg 1, \end{cases} \tag{62}$$

and

$$\sigma_{\ln Y}^2 = \frac{0.20\sigma_R^2}{\left(1 + 0.23\sigma_R^{12/5}\right)^{7/6}} \approx \begin{cases} 0.20\sigma_R^2, & \sigma_R^2 \ll 1, \\ \ln 2, & \sigma_R^2 \gg 1, \end{cases} \tag{63}$$

for a spherical-wave.

For practical applications, such as for FSOC, the irradiance is averaged across the receiver aperture, rather than determined at a single point, and the light is focused

onto a receiver that detects the total power in the aperture. This allows the receiver to capture more energy from the propagating beam, and also averages out the spatially varying scintillation effects. For a Gaussian beam, and assuming Kolmogorov turbulence, the aperture-averaged log-variance of x is [2]

$$\sigma_{\ln x}^2 (D) \cong 0.49\sigma_1^2 \left(\frac{\Omega_G - \Lambda_1}{\Omega_G + \Lambda_1}\right)^2 \left(\frac{1}{3} - \frac{1}{2}\bar{\Theta}_1 + \frac{1}{5}\bar{\Theta}_1^2\right)$$

$$\times \left[\frac{\eta_x}{1 + 0.40\eta_x\left(2 - \bar{\Theta}_1\right)/\left(\Lambda_1 + \Omega_G\right)}\right]^{7/6}, \tag{64}$$

where

$$\eta_x = \frac{\left(\frac{1}{3} - \frac{1}{2}\bar{\Theta}_1 + \frac{1}{5}\bar{\Theta}_1^2\right)^{-6/7} \left(\sigma_B/\sigma_1\right)^{12/7}}{\left(1 + 0.56\sigma_B^{12/5}\right)}. \tag{65}$$

The aperture-averaged log-variance of y is

$$\sigma_{\ln y}^2 (D) \cong \frac{1.27\sigma_1^2\eta_y^{-5/6}}{1 + 0.40\eta_y/\left(\Lambda_1 + \Omega_G\right)}, \quad \eta_y \ll 1, \tag{66}$$

where

$$\eta_y = 3\left(\frac{\sigma_1}{\sigma_B}\right)^{12/5} \left(1 + 0.69\sigma_B^{12/5}\right). \tag{67}$$

The variance is determined via $\sigma_{x,y}^2 = \exp\left(\sigma_{\ln x,y}^2\right) - 1$. The parameter σ_B^2 is the Rytov variance for a beam wave, which is approximated as

$$\sigma_B^2 \cong 3.86\sigma_1^2 \left\{0.40\left[(1 + 2\Theta_1)^2 + 4\Lambda_1^2\right]^{5/12}\right. \tag{68}$$

$$\left. \times \cos\left[\frac{5}{6}\tan^{-1}\left(\frac{1 + 2\Theta_1}{2\Lambda_1}\right)\right] - \frac{11}{16}\Lambda_1^{5/6}\right\} \tag{69}$$

where σ_1^2 is the plane-wave Rytov variance given as $\sigma_1^2 = 1.23C_n^2k^{7/6}L^{11/6}$. The values Θ_1 and Λ_1 are the curvature parameter and Fresnel ratio at the receive plane for vacuum propagation, which given in terms of their respective values at the source

21

plane, are [1]

$$\Theta_1 = \frac{\Theta_0}{\Theta_0^2 + \Lambda_0^2} \tag{70}$$

and

$$\Lambda_1 = \frac{\Lambda_0}{\Theta_0^2 + \Lambda_0^2}. \tag{71}$$

The parameter $\bar{\Theta}_0$ is simply defined as $\bar{\Theta}_0 = 1 - \Theta_0$. Finally, the value Ω_G characterizes the finite size of a Gaussian lens and is given to be $\Omega_G = 2L/kW_G^2$ where $W_G = (D^2/8)^{1/2}$ with D representing the receive aperture diameter.

The temporal nature of atmospheric turbulence is typically described using the Tyler and Greenwood frequencies given by [47]

$$f_T = 0.0586 D^{-1/6} k \left[\int_0^L C_n^2(z) |V|^2 \, \mathrm{d}z \right]^{1/2} \tag{72}$$

$$= 0.0902 \left(\frac{r_0}{D} \right)^{1/6} \left(\frac{|V|}{r_0} \right), \tag{73}$$

and

$$f_G = 0.2542 \left[\int_0^L C_n^2(z) |V|^{5/3} \, \mathrm{d}z \right]^{3/5} \tag{74}$$

$$= 0.426 \frac{|V|}{r_0}, \tag{75}$$

where $|V|$ is the mean wind velocity along the path. The majority of tilt jitter fluctuates at rates below the Tyler frequency. Similarly, the majority of higher-order and lower-order phase disturbances fluctuates at rates below the Greenwood frequency. This provides a design point for tilt and higher-order compensator's closed-loop bandwidths. The wind velocity in Eqs. (72) and (74) is frequently described by

the Bufton wind model given as [1]

$$V(h) = \omega_g h + V_g + 30 \exp\left[-\left(\frac{h - 9400}{4800}\right)^2\right], \tag{76}$$

where V_g is the ground wind speed and ω_g is the slew rate of a ground-based telescope tracking an aerial target.

2.3.3 Turbulence effects on FSOC.

Beam spreading and beam wandering alone, without considering the impact of scintillation, can cause the beam to attenuate and wander off the receiver as a result of atmospheric turbulence. When this occurs, the receiver experiences a fade. For horizontal propagation (constant C_n^2), the Gaussian-beam wander displacement assuming infinite outer scale is [1]

$$\langle r_c^2 \rangle = 2.42 C_n^2 L^3 W_0^{-1/3}{}_2F_1\left(\frac{1}{3}, 1; 4; 1 - |\Theta_0|\right), \tag{77}$$

where $_2F_1$ is a hypergeometric function and Θ_0 is the curvature parameter defined in Eq. (23). When the beam is collimated, $\Theta_0 = 1$, then Eq. (77) reduces to

$$\langle r_c^2 \rangle = 2.42 C_n^2 L^3 W_0^{-1/3}, \tag{78}$$

and when the beam is focused, $\Theta_0 = 0$, then it reduces to

$$\langle r_c^2 \rangle = 2.72 C_n^2 L^3 W_0^{-1/3}. \tag{79}$$

If the turbulence is assumed to be isotropic, then the Cartesian components of the displacement can be treated as identically distributed, zero-mean, Gaussian random

variables x_c and y_c. They are related to the displacement via

$$r_c = \sqrt{x_c^2 + y_c^2}. \tag{80}$$

The variances of x_c and y_c can then be found by

$$\begin{align}
\langle r_c^2 \rangle &= \langle x_c^2 + y_c^2 \rangle, \tag{81} \\
&= \langle x_c^2 \rangle + \langle y_c^2 \rangle, \tag{82} \\
&= \langle x_c^2 \rangle + \langle x_c^2 \rangle, \tag{83} \\
&= 2 \langle x_c^2 \rangle, \tag{84}
\end{align}$$

since $\langle x_c^2 \rangle = \langle y_c^2 \rangle$. The beam displacement follows a Rayleigh distribution with a PDF of

$$f_R(r) = \frac{r}{\sigma^2} \exp\left(\frac{-r^2}{2\sigma^2}\right), \quad r \geq 0, \tag{85}$$

with a cumulative distribution function (CDF) of

$$F_R(r) = \int_{-\infty}^{r} f_R(\xi) \, d\xi = \int_0^r \frac{r}{\sigma^2} \exp\left(\frac{-r^2}{2\sigma^2}\right) = 1 - \exp\left(\frac{-r^2}{2\sigma^2}\right), \tag{86}$$

where $\sigma^2 = \langle x_c^2 \rangle = \langle y_c^2 \rangle = 1/2 \langle r_c^2 \rangle$. By way of example, a collimated Gaussian beam propagating 100km through horizontal turbulence at $C_n^2 = 1 \times 10^{-17} \text{m}^{-2/3}$ with an initial beam waist of $W_0 = 5\text{cm}$, results in a PDF and CDF of displacement shown in Fig. 3.

When combined with the turbulence-induced beam wander, short-term beam radius W_{ST} at the receiver can be used to determine the average irradiance at the
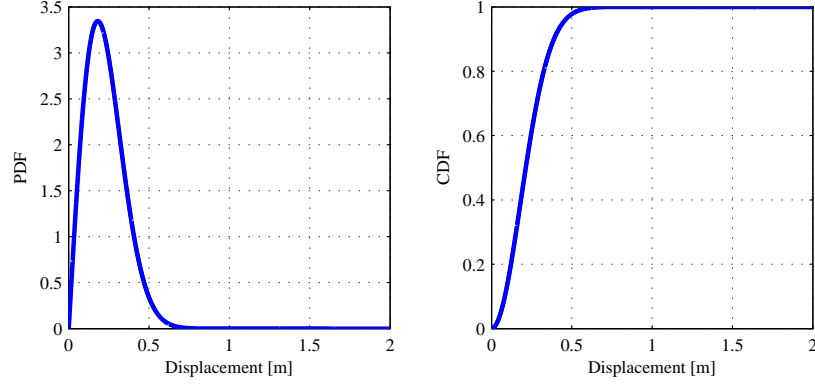
Figure 3. PDF and CDF for 5cm beam propagating 100km.

receiver. The short-term beam radius is given by [1]

$$W_{ST} = W\sqrt{1 + 1.33\sigma_R^2\Lambda^{5/6}\left[1 - 0.66\left(\frac{\Lambda_0}{1 + \Lambda_0^2}\right)^{1/6}\right]}, \qquad (87)$$

for a collimated beam and by

$$W_{ST} = W\sqrt{1 + 0.35\sigma_R^2\Lambda^{5/6}}, \qquad (88)$$

for a focused beam. The long term beam radius can then be found via [1]

$$W_{LT} = \sqrt{W_{ST}^2 + \langle r_c^2 \rangle}, \qquad (89)$$

where r_c^2 is found from Eq. (78) or Eq. (79). Continuing from the previous example, the short term beam radius is $W_{ST} = 1.005$m, the mean-square displacement of the beam's centroid is $\langle r_c^2 \rangle = 0.0657$m^2, and the long term beam radius is $W_{LT} = 1.037$m.

The received power of each possible beam location is found by integrating the displaced received irradiance over a circular telescope pupil. The resulting captured

power $P(x_c, y_c)$ for a beam centered on the Cartesian coordinates (x_c, y_c) is given by

$$
\begin{aligned}
P(x_c, y_c) &= \iint\limits_A I_R(x, y) \, dy \, dx \\
&= \int_{x_c - r_R}^{x_c + r_R} \int_{y_c - \sqrt{r_R^2 - (x - x_c)^2}}^{y_c + \sqrt{r_R^2 - (x - x_c)^2}} \frac{2}{\pi W_{ST}^2} \exp\left[-\frac{2(x^2 + y^2)}{W_{ST}^2} \right] dy \, dx \\
&= \frac{1}{\sqrt{\pi} W_{ST}} \int_{x_c - r_R}^{x_c + r_R} \exp\left(\frac{-x^2}{W_{ST}^2} \right) \\
&\quad \times \left[\operatorname{erf}\left(\frac{y_c + \sqrt{r_R^2 - (x - x_c)^2}}{W_{ST}} \right) \right. \\
&\quad \left. - \operatorname{erf}\left(\frac{y_c - \sqrt{r_R^2 - (x - x_c)^2}}{W_{ST}} \right) \right] dx,
\end{aligned}
\tag{90}
$$

where I_R is the irradiance at the receive plane and A represents the receive aperture area. Relating the received power at a given position and the probability of each position, a CDF can be created. Using the same scenario and turbulence conditions with 1W of transmitted power and a 10cm diameter receiver, the resulting CDF is shown in Fig. 4.

The fade probability is found by determining the probability at the detection threshold. This calculation ignores the higher-order effect of scintillation, which causes spatial variation in intensity across the receive plane. Using wave-optics simulation, a scintillation included CDF can be calculated via numerous independent random realizations of the atmosphere. Using the same scenario and turbulence conditions from before, the resulting CDF is shown in Fig. 5.

In addition to the above method of determining the long-term turbulence-induced beam waist, Andrews and Phillips give the effective beam width W_e as a result of
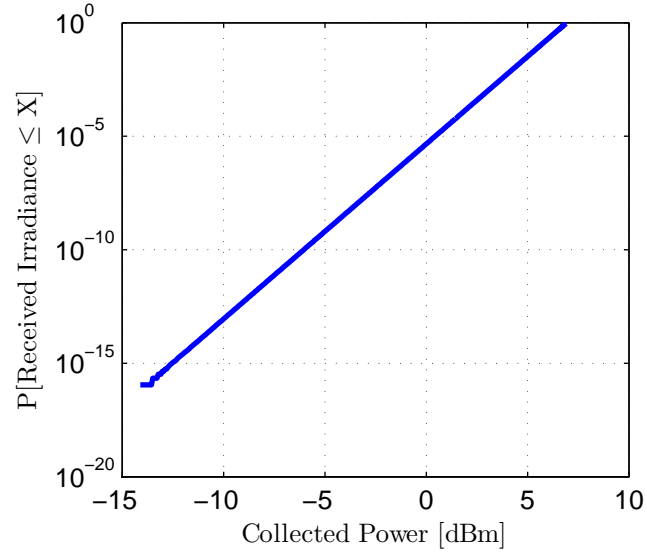
Figure 4. CDF for tilt-only disturbance.
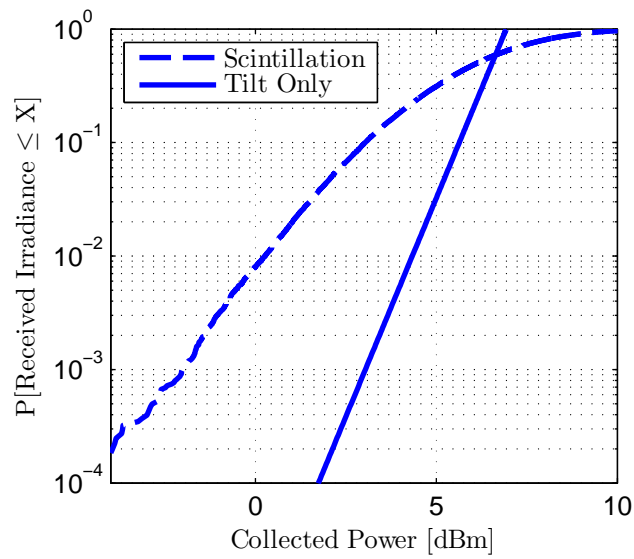
Figure 5. CDF for scintillation included disturbance.

27

propagating through turbulence as [2]

$$W_e = W \left(1 + 1.63\sigma_1^{12/5}\Lambda\right)^{1/2}.$$ (91)

If all of the beam displacement is due to atmospheric turbulence, and not pointing errors induced at the transmitter, then the effective beam waist is the same as the long-term beam waist $W_{LT} = W_e$. This formulation proves useful to calculate the mean irradiance at the receiver plane.

2.3.4 Anisoplanatic separation.

In previous work, Louthain determined the analytic log-amplitude and phase structure functions for a horizontal path starting with the von Kármán PSD

$$\Phi_n (\kappa, z) = \frac{0.033C_n^2 (z)}{\left(\kappa^2 + \kappa_0^2\right)^{11/6}},$$ (92)

where κ is the three-dimensional radial spatial frequency and $\kappa_0 = 2\pi/L_0$ [1, 47]. In general, a structure function associated with a random process $x (t) = \mu_x (t) + x_1 (t)$ is defined by

$$D_x (t_1, t_2) = \left\langle [x (t_1) - x (t_2)]^2 \right\rangle,$$ (93)

where μ_x is the mean value of x. If μ_x is slowly varying, then the difference in the means can be ignored, making it useful for the characterization of random processes with stationary increments such as this. When the process is stationary in the wide sense, then the structure function reduces to

$$D_x (\tau) = 2 [R_x (0) - R_x (\tau)],$$ (94)

where $R_x(\tau)$ is the autocorrelation of $x(t)$. The spatial log-amplitude structure function is

$$
\begin{aligned}
D_\chi(d) &= 3.089 \left(\frac{L_0}{r_0}\right) \\
&\times \int_0^\infty \left[1 - J_0\left(\frac{\kappa d}{L_0}\right)\right] \left[1 - \frac{2\pi L_0^2}{\lambda L \kappa^2} \sin\left(\frac{\lambda L \kappa^2}{2\pi L_0^2}\right)\right] \frac{\kappa d\kappa}{(\kappa^2 + 4\pi^2)^{11/6}}, \quad (95)
\end{aligned}
$$

where d is separation the separation distance between points of interest in the receive plane and J_0 is the zeroth-order Bessel function of the first kind [29, 31]. Similarly the phase structure function is

$$
\begin{aligned}
D_\psi(d) &= 3.089 \left(\frac{L_0}{r_0}\right) \\
&\times \int_0^\infty \left[1 - J_0\left(\frac{\kappa d}{L_0}\right)\right] \left[1 + \frac{2\pi L_0^2}{\lambda L \kappa^2} \sin\left(\frac{\lambda L \kappa^2}{2\pi L_0^2}\right)\right] \frac{\kappa d\kappa}{(\kappa^2 + 4\pi^2)^{11/6}}. \quad (96)
\end{aligned}
$$

The structure functions are plotted together in Fig. 6. Also shown are the separations required for phase anisoplanatism (uncorrelated phase) and tilt anisoplanatism (uncorrelated tilt) which are

$$
\theta_0 = 0.949 \left(k^2 C_n^2 L^{8/3}\right)^{-3/5}, \quad (97)
$$

and

$$
\theta_{TA} = \frac{0.319\lambda D^{1/6}}{C_n L^{3/2}}, \quad (98)
$$

respectively [18, 31]. This shows that two points separated such that they have log-amplitude independence still can tilt globally in a similar manner. This allows a single tracking mechanism to be used for multiple separated beams without sacrificing too much wander between beams. The separation chosen for further analysis is twice the Fresnel zone size of $\rho_c = (L/k)^{1/2}$ where $k = 2\pi/\lambda$ [1]. For this scenario, the

29
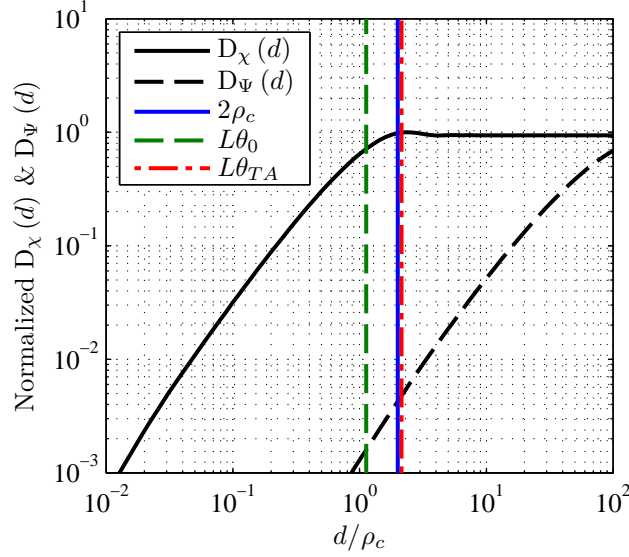
Figure 6. The normalized amplitude and phase structure functions are shown. When the structure function no longer increases with increased separation d, then points separated by that distance are uncorrelated from each other. The vertical lines show the separations due to the isoplanatic angle θ_0, the tilt isoplanatic angle θ_{TA}, and the chosen separation of twice the Fresnel zone size $2\rho_c$.

separation is $2\rho_c = 31.4$cm.

2.3.5 Sums of gamma-gamma random variables.

The received irradiance from a Gaussian beam can be modeled as a Gamma-Gamma random variable. A multiple-beam model can then be treated as a sum of independent Gaussian beams, which can be modeled as a sum of independent Gamma-Gamma random variables. The development of the theoretical approximation for the sum of multiple, independent, identically distributed Gamma-Gamma random variables was recently developed by Chatzidiamantis et al. It begins with the sum of the product of two independent Gamma random variables [8]

$$I_N = \sum_{i=1}^{N} x_i y_i, \tag{99}$$

30

where N is the number of independent beams. This can be rewritten as

$$
\begin{aligned}
I_N &= \frac{1}{N} \left(\sum_{i=1}^{N} x_i \right) \left(\sum_{i=1}^{N} y_i \right) \\
&+ \frac{1}{N} \sum_{i=1}^{N-1} \sum_{j=i+1}^{N} (x_i - x_j)(y_i - y_j).
\end{aligned}
\tag{100}
$$

In this form, the equation is seen to be simply the scaled product of the sum of two Gamma random variables plus an error term ϵ given by

$$
\epsilon = \frac{1}{N} \sum_{i=1}^{N-1} \sum_{j=i+1}^{N} (x_i - x_j)(y_i - y_j).
\tag{101}
$$

Since the Gamma distribution exhibits infinite divisibility each sum of independent, identically distributed Gamma random variables is equivalent to a Gamma random variable with shaping parameters of $\alpha_N = N\alpha$ and $\beta_N = N\beta$, respectively. The two resulting Gamma random variables then have variances of σ_x/N and σ_y/N. Using Eq. (57) and replacing α and β with α_N and β_N produces the new multi-beam PDF approximation. Chatzidiamantis et al. further refined the approximation by accounting for the error term by adding a correction factor to α_N such that

$$
\alpha_N = N\alpha + \epsilon_N.
\tag{102}
$$

The correction factor ϵ_N can be approximated by minimizing the difference between the first four moments generated using the ϵ_N with a single Gamma-Gamma random variable and the moments generated without the correction factor using multinomial expansion for N Gamma-Gamma random variables. Using non-linear regression, the

31

result can be closely approximated to be

$$\epsilon_N = (1 - N) \frac{0.127 + 0.95\alpha + 0.0058\beta}{1 + 0.00124\alpha + 0.98\beta}. \tag{103}$$

2.4 Wave-optics simulations

Chapter IV develops a model for multiple, spatially separated beams based on the work shown in Sections 2.3.4 and 2.3.5. The new model is validated through comparison with digital wave-optics simulation of the beams propagating through optical turbulence.

Wave-optics simulation starts with the Fresnel diffraction integral in Eq. (19). The diffraction integral can be converted into

$$U(x_1, y_1) = U(x_0, y_0) \otimes \left[\frac{e^{ikz}}{i\lambda z} e^{i\frac{k}{2z}\left(x_0^2 + y_0^2\right)} \right] \tag{104}$$

where $U(x_0, y_0)$ is the input field and $\times$ denotes the convolution of the input field with the free-space amplitude spread function [50].

At this point Schmidt introduces operator notation which is useful for writing the equations more compactly [50]. The operators used are:

$$\mathcal{Q}\left[c, \boldsymbol{r}\right]\left\{U\left(r\right)\right\} \equiv e^{i\frac{k}{2}c|\boldsymbol{r}|^2} U\left(r\right) \tag{105}$$

$$\mathcal{V}\left[b, \boldsymbol{r}\right]\left\{U\left(\boldsymbol{r}\right)\right\} \equiv b U\left(b\boldsymbol{r}\right) \tag{106}$$

$$\mathcal{F}\left[\boldsymbol{r}, \boldsymbol{f}\right]\left\{U\left(\boldsymbol{r}\right)\right\} \equiv \int_{-\infty}^{\infty} U\left(\boldsymbol{r}\right) e^{-i2\pi\boldsymbol{f}\cdot\boldsymbol{r}} \mathrm{d}\boldsymbol{r} \tag{107}$$

$$\mathcal{F}^{-1}\left[\boldsymbol{f}, \boldsymbol{r}\right]\left\{U\left(\boldsymbol{f}\right)\right\} \equiv \int_{-\infty}^{\infty} U\left(\boldsymbol{f}\right) e^{i2\pi\boldsymbol{f}\cdot\boldsymbol{r}} \mathrm{d}\boldsymbol{r} \tag{108}$$

$$\mathcal{R}\left[d, \boldsymbol{r}_1, \boldsymbol{r}_2\right]\left\{U\left(\boldsymbol{r}_1\right)\right\} \equiv \frac{1}{i\lambda d} \int_{-\infty}^{\infty} U\left(\boldsymbol{r}_1\right) e^{i\frac{k}{2d}|\boldsymbol{r}_2 - \boldsymbol{r}_1|^2} \mathrm{d}\boldsymbol{r}_1 \tag{109}$$

$$\mathcal{Q}_2\left[d, \boldsymbol{r}\right]\left\{U\left(\boldsymbol{r}\right)\right\} \equiv e^{i\pi^2 \frac{2d}{k}|\boldsymbol{r}|^2} U\left(\boldsymbol{r}\right) = \mathcal{Q}\left[\frac{4\pi^2}{k}d, \boldsymbol{r}\right]\left\{U\left(\boldsymbol{r}\right)\right\}. \tag{110}$$

32

Using this notation Eq. (104) becomes

$$U(\boldsymbol{r}_2) = \mathcal{F}^{-1}[\boldsymbol{r}_2, \boldsymbol{f}_1] \, H(\boldsymbol{f}_1) \, \mathcal{F}[\boldsymbol{f}_1, \boldsymbol{r}_1] \, \{U(\boldsymbol{r}_1)\}, \tag{111}$$

where $H(\boldsymbol{f})$ is the transfer function of free-space propagation given by

$$H(\boldsymbol{f}_1) = e^{ikz} e^{-i\pi\lambda z \left(f_{X1}^2 + f_{Y1}^2\right)}. \tag{112}$$

This technique, known as the angular-spectrum method, is used by the wave-optics simulation software WaveProp (Matlab toolbox provided by the Optical Sciences Company) [57]. To accommodate different grid resolutions between the input and output planes, the scaling factor $m = \delta_1/\delta_2$ is used, where δ_1 and δ_2 are the grid spacings used in the numerical representation of the input and output planes respectively. Using the operator notation above and noting that $\pm m$ may be used in the angular-spectrum form of diffraction, Eq. (111) becomes

$$\begin{aligned}
U(\boldsymbol{r}_2) &= \mathcal{Q}\left[\frac{m-1}{m\Delta z}, \boldsymbol{r}_2\right] \mathcal{F}^{-1}\left[\boldsymbol{f}_1, \frac{\boldsymbol{r}_2}{m}\right] \mathcal{Q}_2\left[-\frac{\Delta z}{m}, \boldsymbol{f}_1\right] \\
&\quad \times \mathcal{F}[\boldsymbol{r}_1, \boldsymbol{f}_1] \mathcal{Q}\left[\frac{1-m}{\Delta z}, \boldsymbol{r}_1\right] \frac{1}{m} \{U(\boldsymbol{r}_1)\} \tag{113} \\
&= \mathcal{Q}\left[-\frac{m-1}{m\Delta z}, \boldsymbol{r}_2\right] \mathcal{F}^{-1}\left[\boldsymbol{f}_1, \frac{\boldsymbol{r}_2}{m}\right] \mathcal{Q}_2\left[\frac{\Delta z}{m}, \boldsymbol{f}_1\right] \\
&\quad \times \mathcal{F}[\boldsymbol{r}_1, \boldsymbol{f}_1] \mathcal{Q}\left[-\frac{1-m}{\Delta z}, \boldsymbol{r}_1\right] \frac{-1}{m} \{U(\boldsymbol{r}_1)\}. \tag{114}
\end{aligned}$$

The simulation propagates the fields from one plane to the next via Eq. (113). To

satisfy Nyquist sampling requirements the inequalities [13, 50]

$$\delta_n \leq \frac{\lambda z - D_n \delta_1}{D_1} \tag{115}$$

$$N \geq \frac{D_1}{2\delta_1} + \frac{D_n}{2\delta_n} + \frac{\lambda \Delta z}{2\delta_1 \delta_n} \tag{116}$$

$$\Delta z_i \leq \frac{\min(\delta_1, \delta_n)^2 N}{\lambda} \tag{117}$$

are used. The parameters δ_1 and δ_n are the grid spacing sizes at the initial plane and the final plane with $n - 1$ partial propagations, D_1 and D_n are the diameters of the areas of interest at the first and last plane, and N is the number of grid points across the field. To determine the appropriate propagation grid parameter first N, δ_1, and δ_n are chosen based on the first two equations then choose the minimum number of partial propagations by using the third equation resulting in at least $n = \text{ceil}(\Delta z/\Delta z_{\max}) + 1$ partial propagations. It should be noted that the number of partial propagations can always be increased by using smaller partial propagation distances.

To simulate the effects of turbulence, random phase-screens are added to the fields after each propagation step. This collapses the phase effects of each partial propagation into a discrete representation. To ensure that the receive area of interest captures the necessary amount of light, D_1 and D_2 are replaced with

$$D_1' = D_1 + c\frac{\lambda \Delta z}{r_{0,rev}} \tag{118}$$

$$D_2' = D_2 + c\frac{\lambda \Delta z}{r_0}, \tag{119}$$

where $r_{0,rev}$ is the coherence diameter computed for light propagating in the reverse direction and c is an adjustable parameter. Values of c range from 2 to 8 with $c = 2$ capturing 97% of the light. The sampling analysis then can be redone using D_1' and

D'_2 in place of D_1 and D_2 respectively.

III. Previous Work

Research for improving the effectiveness of free-space laser communications systems encompasses several fields. The research focuses on those fields most applicable to an airborne FSOC system. The airborne application requires simplicity and a small footprint, both in size and weight, while providing the most availability over a wide range of conditions. To take full advantage of the benefits of FSOC, an integrated approach is required. In this manner, each component of current FSOC research is surveyed with the intention of identifying areas of improvement or applicability to the research.

The first area of research involves optimizing the transmitter and receiver for the the FSOC application when considering the effects of atmospheric turbulence. Next, various diversity techniques are considered that attempt to average out the spatial and temporal variations at the receiver. After that, some wavefront control techniques including lower-order techniques such as tilt correction are considered. These three areas deal primarily with mitigating the occurrence of intensity fades at the receiver caused by atmospheric turbulence. In an attempt to mitigate the impact of intensity fades, the use of various modulation schemes is investigated.

3.1 Transmitter/receiver design

The design of the transmitter and receiver plays a large role in the overall effectiveness of a FSOC system. The trade off between between beam size and beam wander was shown by Churnside [10]. His results showed that in weak turbulence, the intensity fluctuations can be reduced by adjusting the beam size. Yenice et al. proposed a scheme that adaptively adjusts the beam size based the observed turbulence conditions [66, 67]. By adjusting the beam size based on the atmospheric

conditions, the effects of turbulence can be minimized. More recently, it was shown that a linear array of Gaussian beams propagated through turbulence, with spreads adjusted sufficiently, can have the same angular spread as a single Gaussian beam propagated through a vacuum, with the same angular spread, along the dimension of the array [25, 28]. While optimizing the angular spread to minimize the effects of turbulence is desirable, those benefits must always be weighed against the cost of increased beam size which would decrease the average power incident on the receiver [58].

Another way to reduce the impact of atmospheric turbulence on a propagated beam is through decreasing the beam's spatial coherence. In addition to spreading out the beam, the reduced coherence also reduces the intensity fluctuations caused by constructive and destructive interference of the beam with itself as it propagates through the turbulence [45,46]. While the speckle reduction is beneficial, the increased beam spread can result in less power at the receiver, particularly for very long paths. Recent work has examined the respective trade offs and has attempted to optimize the received intensity [9].

On the receiver side, the most obvious method to increase to total power received is to increase the aperture size. Additionally, as the aperture size increases, the fluctuations decrease, especially as the size of the receive aperture increases beyond the correlation width $\rho_c = (L/k)^{-1/2}$ for a collimated beam. For larger apertures, the beam experiences uncorrelated intensity variations due to turbulence over the aperture. Whether one assumes direct detection across the aperture, or the incident light is focused onto a detector or coupled onto a fiber, the variations are averaged out, a phenomenon commonly referred to as aperture averaging. The phenomenon has been studied extensively to determine the performance improvements and the probability distribution of the received intensity [11, 17, 43, 69–72]. Zhao et al. showed the

relationship between receiver size and propagation distance and determined optimal aperture sizes based on propagation distance and turbulence strength [74]. Other recent work showed good agreement between the lognormal PDF and wave-optics simulations under weak scintillation conditions while the gamma-gamma PDF agreed with wave-optics simulations under weak and moderate scintillation [34]. For the research described in Chapters IV–VI, the aperture size is fixed.

When the incident light is coupled into a fiber, the signal typically needs to be amplified, either optically or electrically. An erbium-doped fiber amplifier (EDFA), which optically enhances the signal but is susceptible to increased noise due to spontaneous emission, increases the power at the detector [22]. Additional investigations showed that optical-preamplification of 30dB was strong enough to overcome thermal noise while still being below the shot noise [42]. Another method of amplifying the signal uses an avalanche photo diode (APD), which avoids noise resulting from spontaneous emission but introduces avalanche noise [24]. The research models the combined noise effects as AWGN, as well as direct detection models and detectors without amplification.

3.2   Diversity techniques

Diversity techniques take advantage of the spatial and temporal variations in atmospheric conditions and average the result. This includes using multiple transmitters, multiple receivers, and time interleaving, with the goal of propagating beams through independent paths to average out the effect of turbulence. Spatial diversity, as seen in the previous section, can be accomplished through manipulation of the transmitted beam size or the receive aperture size [1, 2]. Much research has been done on multiple transmitters and multiple receivers [7, 23, 35, 40, 48]. Both of these techniques take advantage of the uncorrelated spatial atmospheric effects to average

out the intensity variations. Chatzidiamatis et al. combined the use of multiple transmitters and multiple receivers as the motivation for developing a model for the sum of N independent Gamma-Gamma random variables [8]. Finally, since different wavelengths diffract differently, over a long path beams of different wavelengths can be combined to average out the effects of turbulence [39].

Recent work by Louthain and Schmidt developed a theoretical basis for the separation required for two points to scintillate independently [31, 33]. Their work showed that a separation distance of one to three times the Fresnel zone size ρ_c would result in anisoplanatic scintillation of two points. The variation depends primarily on the initial beam conditions, with a collimated beam having an anisoplanatic separation of $2\rho_c$. The research in the later chapters uses this separation and applies it more than two transmitters to ensure that each transmitter is anisoplanatic from every other transmitter.

3.3 Wavefront control

Wavefront control systems use measurements of the incident light to correct for wavefront aberrations in real time to compensate for distortions that arise from propagation through the turbulent atmosphere. A wavefront control system can be implemented on either or both ends of the transmission path. On the transmitter side a reference beam, typically a point source, located at the receiver end is used to measure the phase aberrations via a wavefront sensor on the transmitter end. The conjugate of the phase is then imparted on the outgoing beam whereby propagation in the atmosphere subsequently removes it. To implement corrections on the receiver end, a reference at the transmitter is used, sometimes the transmit beam itself. In this case, the conjugate phase is applied prior to the detector or fiber coupler. Typically wavefront correction systems separate measurement and compensation for tilt

from the higher-order aberrations. Tilt causes the beam to wander and accounts for 84% of the total beam distortion, while the higher-order aberrations cause the beam to break up [47, 49, 60].

Compensation for tilt aberrations includes tracking, pointing, and jitter control. Tracking refers to the real-time estimation on compensation to ensure that the received beam is centered on the receiver and occurs on the receiver end. Pointing refers to directing the beam in a manner that ensures the outgoing beam is centered on the target. Jitter control refers to compensating for the platform vibrations and can occur at either end. However, due to the transmission length, small vibrations at the transmitter could result in large deviations at the receiver. For example, a 10 μrad deviation at the transmitter could result in a 1 meter beam movement for a 100 km path. Recent research has shown great capability with only tilt compensation for ground to space optical communications [27]. Crabtree showed that using a peak tracker, as opposed to a traditional centroid tracker or adaptive optics, can significantly reduce fade probability [14]. Other techniques to compensate for jitter include optimizing the beam divergence and using multiple receive apertures with weighted gains to minimize the BER [4, 58]. Most of these techniques concentrate on ground to space optical communications where tilt disturbances, mainly due to jitter, dominate.

Higher-order adaptive optics has been shown to reduce the BER experimentally [61, 62]. The goal here is to reduce scintillation and therefore signal fades by compensating for atmospheric turbulence. Additionally, adaptive optics can be used to maximize fiber coupling efficiency [64]. The research in Chapters IV–VI attempts to minimize the effect of atmospheric turbulence through signal diversity without the use of complicated higher-order wavefront control schemes.

3.4 Modulation techniques

The performance of a FSOC system is not only dependent on the power received, but also on the type of modulation scheme used. The two broad categories of modulation are coherent and incoherent. Coherent techniques encode the information of the light similar to RF systems and require very precise timing. Incoherent techniques vary the transmitted power without the need of precise timing. Both types of modulations have their strengths and weaknesses.

The need for precise timing in coherent techniques arises from the high frequency of light. However, this provides the potential for extraordinary theoretical data rates. Lange et al. demonstrated a 5.625 Gbit/s link over a 142km terrestrial path using binary phase-shift keying (BPSK) [26]. They used a beacon and tracking system resulting in a BER between 10^{-4} and 10^{-6} and showed the potential robustness of a coherent link, even in the atmosphere. Other research has shown that using multiple transmitters in concert with a heterodyne modulations scheme can also improve BER performance [22].

Incoherent, or direct detection, modulates the transmitted power, the simplest being OOK [41]. In this binary digital communication scheme, a '1' and '0' are represented by a pulse of light or the absence of a pulse. The advantage in simplicity is countered by the fact that fades due to turbulence could result in pulses not being detected. Variable threshold techniques have been proposed to address this problem [33]. Another technique is polarization shift keying (PolSK) [59, 73]. This method takes advantage of the isotropic nature of turbulence, which does not affect the polarization of the transmitted signal. In this case, the intensity fades due to turbulence affect all symbols equally. For a binary signaling scheme, this allows for a comparison between two signals, as opposed to a comparison against a threshold. Similarly, pulse position modulation (PPM) uses a pulse at different temporal posi-

tions within a symbol and compares the power detected at each position [35]. PPM takes advantage of the fact that transmitted symbols are much shorter in duration than the rate of change of the turbulence. The disadvantage is the more complex timing and detection scheme required.

For those situations where signal fades can completely disrupt an optical link, hybrid solutions have been investigated [15]. This uses an optical link when available and switches to an RF method when the BER gets too high. For the research described later, OOK with a single transmitter is used as a baseline, but is compared with OOK and PPM combined with multiple transmitters.

3.5 Post processing

Once the symbol is received and the bit estimate is determined, any resulting error would need to be detected or corrected to ensure effective communications. Numerous forward error correction (FEC) codes, originally developed for RF channels, have been investigated for their use with FSOC. Various block, convolutional, Turbo, and Reed-Solomon codes all showed improvements [38,68,76]. Zhao et al. showed that for relatively weak fading channels, the use of Reed-Solomon encoding can improve BER performance to nearly that of a fade-free channel [75]. Other research investigated the use of FEC with the use of multiple transmitters [3,22]. Because most of these techniques were originally developed for RF systems which primarily experience AWGN, they may not provide the best solution for FSOC. FSOC systems experience fades which produces periods of reduced performance. Any FEC or other post processing technique should take this into account, minimizing the impact of fades.

This research described later focuses primarily on the atmospheric transmission and symbol detection aspects of the FSOC system. Improvements in these areas result in a reduced BER. While the use of FEC is not part of this research, it is

conceded that any FEC implementation on top of the techniques considered would only serve to further reduce the overall BER.

IV. Irradiance Modelling

The effects of atmospheric turbulence, as they pertain to a FSOC system, include the effects of scintillation of the propagating beam. These intensity fluctuations vary spatially, as well as temporally along the propagation path. If the overall intensity of the beam were simply to increase, it would still not address the issues associated with the deep fades. These deep fades ultimately impact the receiver's ability to estimate the digital signal, degrading overall communications system performance.

The first approach investigated here to address the problem of signal fades uses multiple, incoherent, independent beams to "average out" the fades. The basic premise is to take advantage of multiple beams, traveling through independent atmospheric channels, which would be unlikely to all experience fades at the same time. Using independent beams provides a best-case scenario which bounds the performance of any multiple transmitter system [55]. This chapter begins with an analytical model of multiple independent beams, and then compares the model to a wave-optics simulation for a given scenario. Once the independent beam case is developed the multiple, spatially separated beam (and correspondingly partially correlated) case is addressed. First a model for the PDF of multiple beams is shown, followed by a comparison to wave-optics simulations.

4.1 Independent beams

Previously, the statistics of a single aperture-averaged Gaussian beam propagating through turbulence was developed. The case of multiple independent provides a limiting case for multiple beams. By using the solution for multiple, independent, identically distributed Gamma-Gamma random variables developed by Chatzidiamantis combined with the shaping parameters derived from the aperture averaged
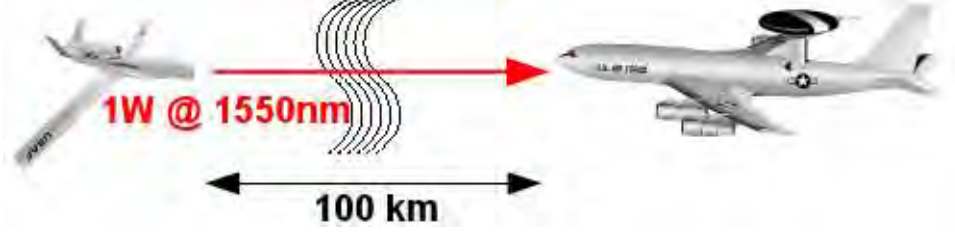
Figure 7. Basic scenario description.

irradiance shown in Eq. (64) and Eq. (66), a bounding model for multi-beam FSOC is derived. This model bounds the performance for multiple transmitters by producing a best-case scenario where each beam is completely independent, and therefore maximizing the averaging effect between beams.

4.1.1 Simulation description.

A wave-optics simulation of a nominal FSOC system was performed using the angular-spectrum method to evaluate the Fresnel diffraction integral [50]. The simulation was designed to simulate uncorrelated beams propagating through turbulence, but done in such a way that there was an easy extension to partially correlated beams. The scenario and propagation grids were designed with this ultimate intent in account.

The scenario for the simulation emulates a nominal FSOC system shown in Fig. 7. A basic list of the parameters used in the simulation is shown in Table 1. The turbulence strength of $C_n^2 = 1 \times 10^{-17} \mathrm{m}^{-2/3}$ equates to an altitude of 13.5km using the Hufnagel-Valley turbulence profile.

4.1.2 Propagation setup and verification.

The sampling requirements were determined using the methods outlined by Coy to avoid aliasing while still adequately sampling the field in the telescope pupil [13]. Using Eqs. (115)–(119) a Matlab routine was developed to simplify the sampling

Table 1. Simulation Parameters.

Parameter	Value
Transmitter Power, P	1W
Transmitter Gaussian Beam Waist, W_0	5cm
Detector Diameter, d_{det}	10cm
Wavelength, λ	1550nm
Index of Refraction Structure Constant, C_n^2	$1.0 \times 10^{-17} \mathrm{m}^{-2/3}$
Path Length, L	100km

analysis process. Fig. 8 shows the implemented routine which gives a contour plot of the required grid size for the transmitter and receiver grid spacings. The process resulted in a chosen transmitter grid spacing of 24.3mm and a receiver grid spacing of 7.3mm along with a required grid size of $2^9 = 512$ points across the grid. Some preliminary testing showed that using a 512×512 grid still introduced small amounts of aliasing so a 1024×1024 grid (the next size up) was used instead. Using the larger grid size and a propagation distance of 100km, Eq. (117) resulted in a minimum of 4 propagation steps.

To verify the simulation, a pair of mutually incoherent Gaussian sources were vacuum-propagated to the receive plane and the resulting irradiance was compared with the propagated irradiance using Eqs. (24)–(27). The beams were separated by a distance of $2\rho_c = 31.4$cm. Fig. 9 shows that the simulated and analytical irradiance profiles compare favorably. Due to the propagation distance, beam divergence, and small separation, the two beams cannot be resolved but instead almost appear like a single Gaussian beam.

Finally, the phase screen generation was verified by comparing the phase structure function of the phase screens with the theoretical structure function of

$$D_\phi \left(r \right) = 6.88 \left(\frac{r}{r_0} \right)^{5/3}. \tag{120}$$

Since the simulation scenario used a constant turbulence strength along the path
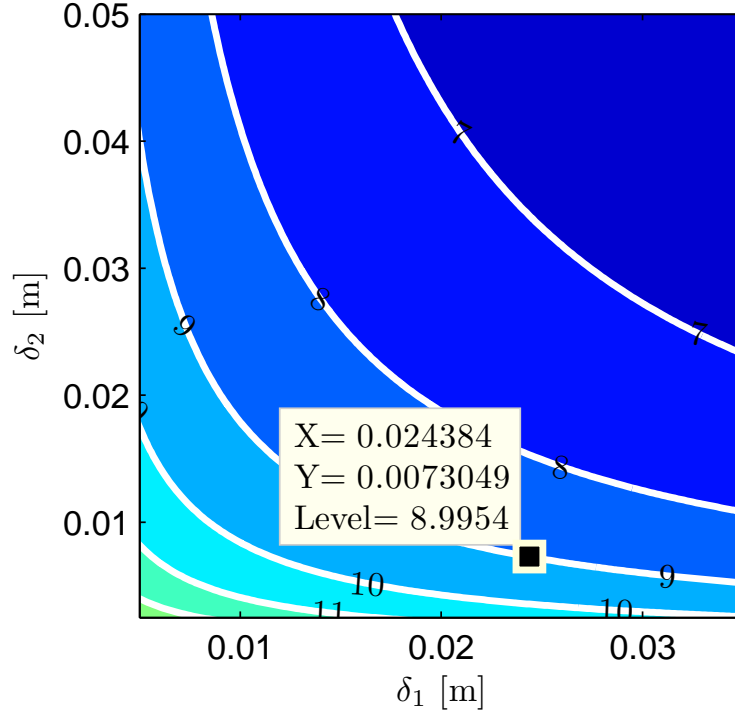
Figure 8. Sampling analysis for wave-optics simulations. The figure is a contour plot of the required grid size given the transmitter spacing (along the x-axis) and receiver spacing (along the y-axis). The contours are shown as $\log_2(N)$. Chosen grid spacing shows 2.4cm for the transmitter plane and 7.3mm for the receiver plane. The analysis determined that a grid size of 512×512 was sufficient, however 1024×1024 was ultimately used.

Figure 9. Comparison of the simulated and analytical irradiance profile for a pair of vacuum-propagated beams.
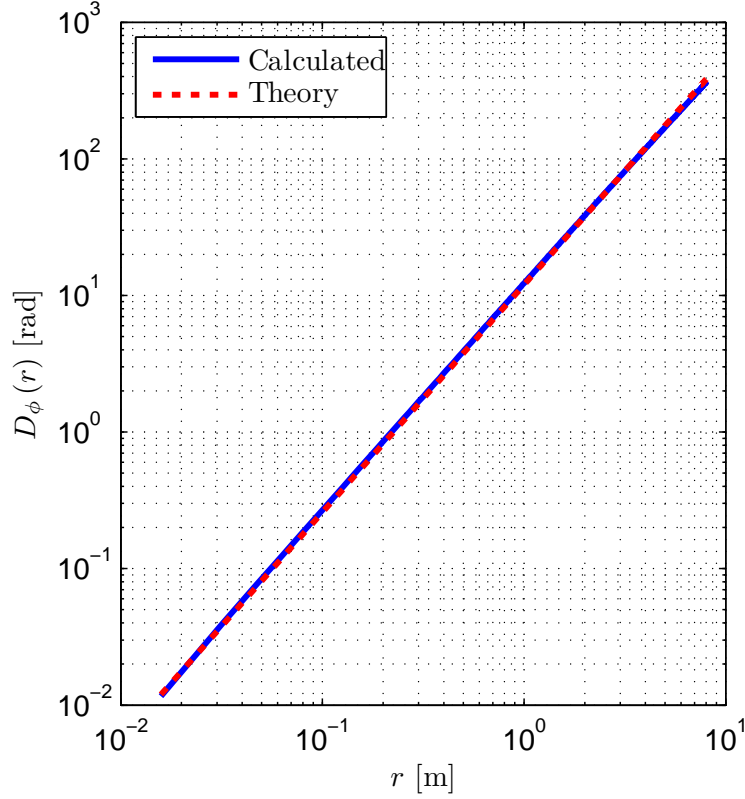
Figure 10. Comparison of the phase structure function from the randomly drawn phase screens and analytical model. The calculated line was generated from 100 random realizations of all phase screens spaced evenly along the path.

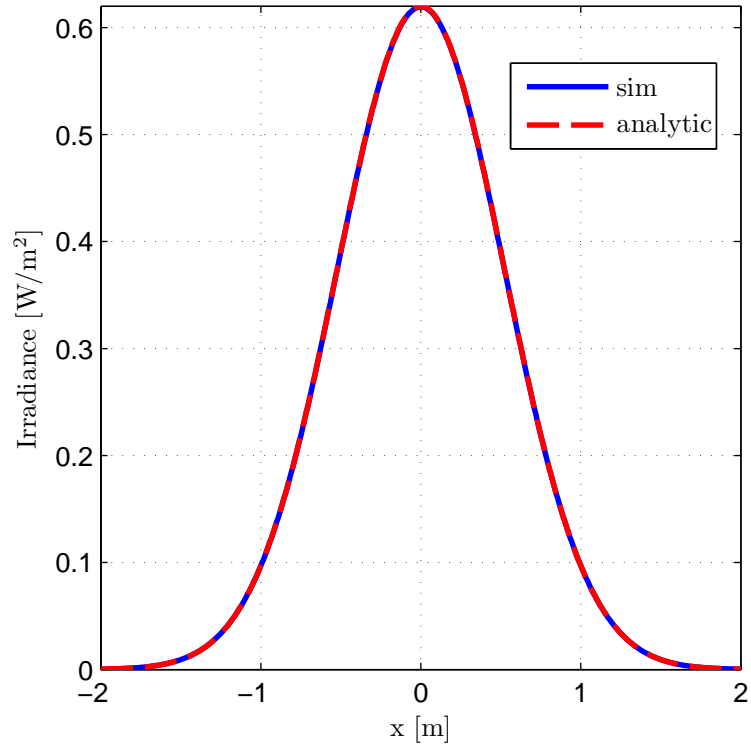and the phase screens were equally spaced between the transmitter and receiver, each phase screen has the same correlation distance or r_0 value. Therefore, the comparison was done using all of the phase screens along the path. Fig. 10 shows the verification of the phase screen correlation properties via the structure function.

4.1.2.1 Processing the propagated beams.

For this simulation, the initially collimated Gaussian beam was transmitted through random realizations of the atmosphere. The resulting irradiance at the receive plane, collected as a two-dimensional grid of irradiances, was masked based on the size of the receive aperture. Data points outside the aperture were multiplied by zero, while

points within the aperture were multiplied by one. The resulting irradiance profile was then integrated in both dimensions of the grid to produce a single total received power across the aperture. The total received power then represented a single data point. Another random realization was produced, resulting in another data point, and so on creating n single-beam received powers.

To create multi-beam results, the received powers were combined in groups of N to correspond with an N-beam transmitter. For example, for dual-beam results the first two received powers were averaged for one data point, the third and fourth irradiances were averaged for the next data point, and so on until all of the irradiances were considered. Using this method creates n/N data points for N beams. The data points were then sorted from lowest to highest. By assigning each data point a marginal probability of N/n a CDF was created.

4.1.3 Comparison of model and simulation.

A comparison between the aperture-averaged Gamma-Gamma CDF from Eq. (64) using α and β resulting from Eqs. (58) and (66) with a wave-optics simulation for a single beam, nominal FSOC system is shown in Fig. 11. The single-beam results show that the well-established analytical model for a single beam produces a good fit to the simulation data. This further confirms that the simulation is sufficiently modeling the engagement scenario.

The results shown in Fig. 12 for one to seven beams show good agreement with the model and also demonstrate a decrease in fade probability as the number of transmitters are increased. It also shows that the marginal improvement decreased as the number of beams used increased. The improvement between one beam and two beams at a cumulative probability of 10^{-3} is 3.02dBm. However, the difference between two and four beams is only 1.95dBm and the difference between four and
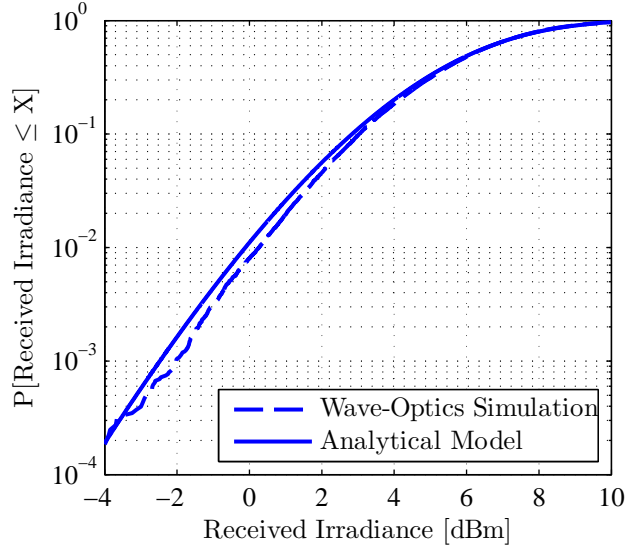
Figure 11. Analytical and wave-optics generated CDF for an aperture-averaged, single beam irradiance.

seven beams is only 1.08dBm. Using multiple transmitters appears to be an effective way of reducing fades, but there seems to be a point of diminishing returns.

The uncorrelated beam case provides a useful best-case scenario for multi-beam transmitters. Exploring the effects of and establishing a model for partially correlated beams adds further realism to this study.

4.2   Partially correlated beams

Practical application of a multi-beam transmitter requires some finite spatial separation between the beams. This means that the beams would not be independent from each other, but partially correlated. This section develops another model to address this partially correlated case. Following that, another comparison to simulation is performed.
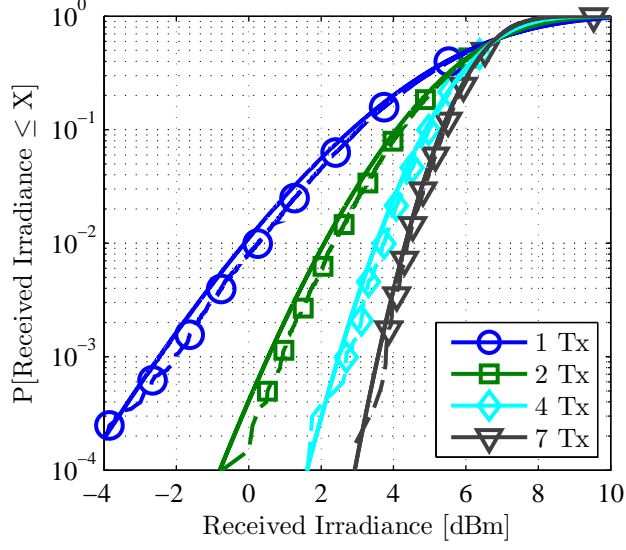
Figure 12. Analytical CDF, solid lines, and wave-optics results, dashed lines. Results are shown for one, two, four, and seven beams based on the number of beams used in the spatially separated, multiple beam configuration.

4.2.1 Beam configuration.

To minimize the amount of area occupied by the multiple transmitters, a hexagonal close-pack spacing is used [54, 56]. Fig. 13 shows the arrangement and relative intensities of each of the patterns. Each pattern used is centered in relation to the single beam. The closest any two beams can be is the chosen separation distance, in this case $2\rho_c$. For the larger number of transmitters, particularly five or more, the maximum separation between the furthest spaced beams is twice the chosen separation distance or $4\rho_c$. Those beams begin to wander independently, since they are spaced further than the spacing required for tilt isoplanatism, which would limit the ability to use a single tracking sensor for beam steering. A simple solution would be to track each beam individually at the cost of increased system complexity. Additionally, regardless of the number of transmitters used, the average power is held constant, which in this scenario is $P = 1\text{W}$.
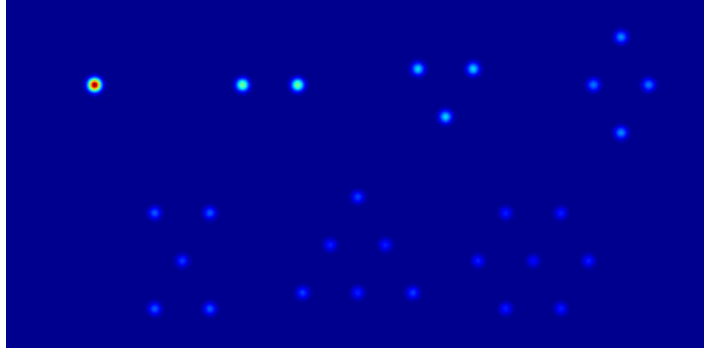
Figure 13. The configuration used for multiple transmitters. Each configuration is a subset of a hexagonal close-pack grid. The top row shows one, two, three, and four transmitters from left to right, while the bottom row shows five, six, and seven transmitters. In all cases, the total average power across all transmitters is held constant.

4.2.2   Model development.

To account for the finite beam separation, a method needed to be developed to account for the partially correlated scintillation resulting from several beams. The independent, identically distributed shaping parameters can be rewritten as

$$\alpha_N = \alpha \left[\frac{N\alpha + \epsilon}{\alpha} \right] \tag{121}$$

$$\beta_N = \beta N, \tag{122}$$

which treats the modification to a single beam shaping parameter as a simple gain. There are then two limiting cases that were considered, perfectly correlated beams and perfectly uncorrelated beams. For perfectly correlated beams the shaping parameter for multiple beams should be the same as for a single beam. For perfectly uncorrelated beams the shaping parameter for multiple beams should be the same as for uncorrelated beams. By raising the gain to a function of the correlation coefficient

the partially correlated shaping parameters become

$$\alpha_N = \alpha \left[\frac{N\alpha + \epsilon}{\alpha} \right]^{f(\rho)} \tag{123}$$

$$\beta_N = \beta N^{f(\rho)}. \tag{124}$$

To satisfy the limiting cases then

$$\lim_{\rho \to 0} f(\rho) = 1, \tag{125}$$

and

$$\lim_{\rho \to 1} f(\rho) = 0. \tag{126}$$

The correlation coefficient itself is a function of beam separation resulting in

$$\alpha_N = \alpha \left[\frac{N\alpha + \epsilon}{\alpha} \right]^{f(\rho(d))} \tag{127}$$

$$\beta_N = \beta N^{f(\rho(d))}, \tag{128}$$

and has limiting cases of

$$\lim_{d \to 0} \rho(d) = 1, \tag{129}$$

and

$$\lim_{d \to \infty} \rho(d) = 0. \tag{130}$$

The correlation coefficient $\rho(d)$ was determined using wave-optics simulations of Gaussian beam pairs of various separation distances propagated over the simulated distance and integrated over a common aperture located between the propagated beams at the receive plane. The resulting relationship between separation distance

54

and correlation coefficient was determined via

$$\rho\left(d\right) = \frac{\left\langle \left(I_A\left(-d/2, 0\right) - \mu_{I_A}\left(-d/2, 0\right)\right)\left(I_A\left(d/2, 0\right) - \mu_{I_A}\left(d/2, 0\right)\right)\right\rangle}{\sigma_{I_A}\left(-d/2, 0\right)\sigma_{I_A}\left(d/2, 0\right)}, \qquad (131)$$

where $\left\langle \cdot \right\rangle$ is the expectation operator and $I_A\left(x, y\right)$ is the received irradiance integrated over the receive aperture for a Gaussian beam centered on x, y and $\mu_{I_A}\left(x, y\right)$ and $\sigma_{I_A}\left(x, y\right)$ are the mean and variance of $I_A\left(x, y\right)$ respectively. The integrated irradiance for each beam was determined using Eq. (90) with the short-term beam waist W_{ST} replaced by the long-term beam waist W_{LT}. The simulated results are shown in Fig. 14 along with first-order results for a single-parameter functional fit of

$$\rho\left(d\right) \approx \exp\left(-0.6875 d/\rho_c\right). \qquad (132)$$

The value of -0.6875 in the model was determined by minimizing the integrated mean squared difference between the model and wave-optics results. This functional form also provides the appropriate limiting conditions as d approaches zero and infinity.

The same simulation data were then used to produce CDFs of the integrated irradiance over the receive aperture for two beams at various separations. Analytical CDFs using the shaping parameters in Eqs. (127) and (128) were then produced using an value for $f\left(\rho\left(d\right)\right)$ which minimized in integrated mean squared difference between the analytical CDF and the wave-optics produced CDF. The resulting $f\left(\rho\left(d\right)\right)$ is plotted against separation distance between the beams in Fig. 15. A model of $\left(\rho\left(d\right)\right)$ is also shown in Fig. 15 such that

$$f\left(\rho\left(d\right)\right) \approx \left(1 - \rho\left(d\right)\right)^{1.4894}, \qquad (133)$$

where the value of 1.4894 was determined by minimizing the integrated mean squared
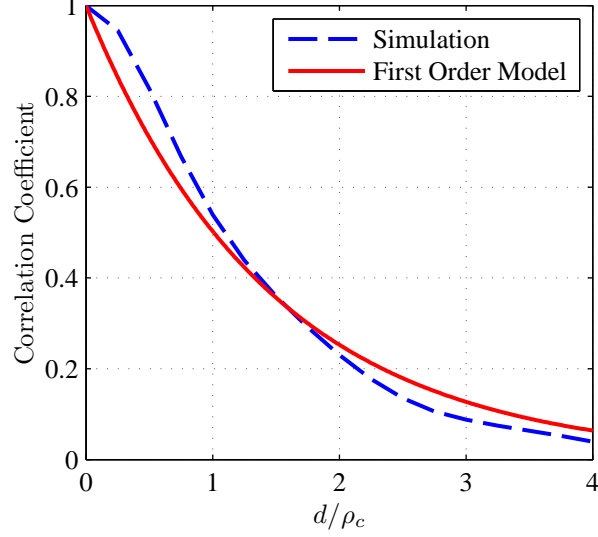
Figure 14. Correlation coefficient versus beam separation for two Gaussian beams propagated over 100km path with $\sigma_1^2 = 1.0$.

difference between the model and simulation results. Combining Eqs. (132) and (133) results in

$$f\left(\rho\left(d\right)\right) \approx \left[1 - \exp\left(-0.6875d/\rho_c\right)\right]^{1.4894}. \tag{134}$$

The simulation results in Fig. 15 show that at a separation distance greater than $3\rho_c$ the value of $f\left(\rho\left(d\right)\right)$ begins to decrease. The aperture-averaged model for the Gamma-Gamma shaping parameter assumes the receive aperture is centered on the beam center. As the beam separation increases, this assumption becomes less valid. To investigate the impact of the displacement on the CDF, several normalized CDFs were created from simulation data with varying receiver displacements. The resulting plot shown in Fig. 16 indicates that there is a slight ~ 0.1dBm shift in the CDF at a probability of 10^{-2}. This error source is small when compared to the CDF shift associated with increasing the number of transmitters, which is on the order of 1.0dBm. The results show that the Gamma-Gamma CDF used for single-beam propagation adequately models off axis irradiance statistics as well.

56
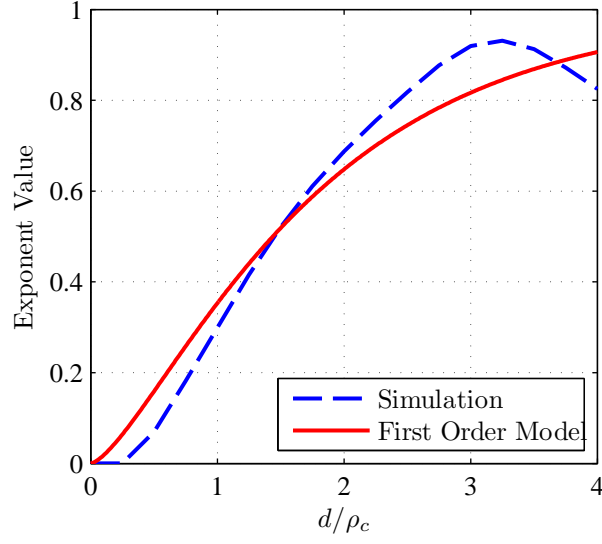
Figure 15. Exponent value $f\left(\rho\left(d\right)\right)$ **in Eqs.** (127) **and** (128) **plotted as a function of beam separation for two Gaussian beams propagated over 100km path with** $\sigma_1^2 = 1.0$.
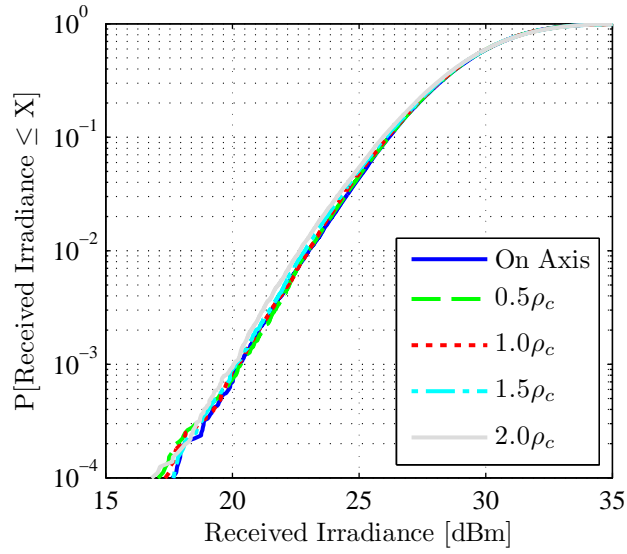

Figure 16. Normalized CDFs for integrated irradiance with receivers placed at various off-axis distances.
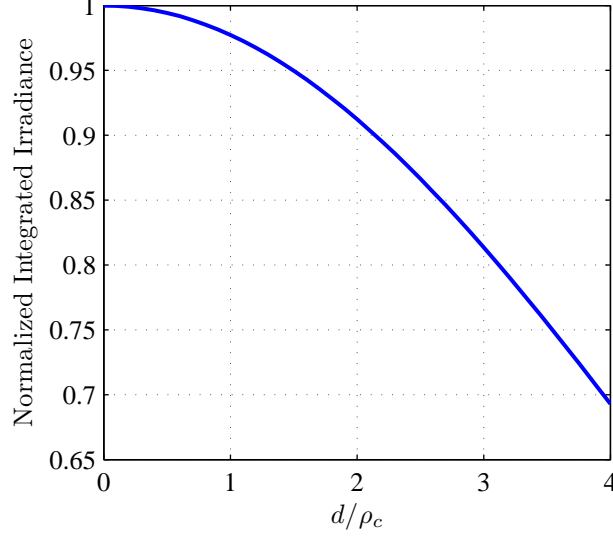
Figure 17. Mean integrated irradiance plotted as a function of receiver distance from beam center.

Another potential source of the decreasing value of $f(\rho)$ beyond $3\rho_c$ in Fig. 15 is the variation in mean received irradiance as a function of receiver displacement from beam center. Fig. 17 demonstrates that as the receiver displacement increases, the mean irradiance decreases. This, coupled with a corresponding decrease in the variance as displacement is increased, provides a partial explanation for the downward trend evident in Fig. 15. However, the primary region of interest lies between $1\rho_c$ and $3\rho_c$ where there is sufficient beam separation to average the irradiance between beams but still close enough for practical applications. At this separation distance there is still reasonable agreement between the simulation data and the model shown in Fig. 15.

Finally, the model also assumes that each beam has the same separation distance from every other beam. While this is true for two or three beams, this assumption is not true for four or more beams. However, the beam configuration shown in Fig. 13 ensures that beams are no closer than the chosen separation distance. Additionally the correlation coefficient as a function of separation distance shown in Fig. 14 indi-

58
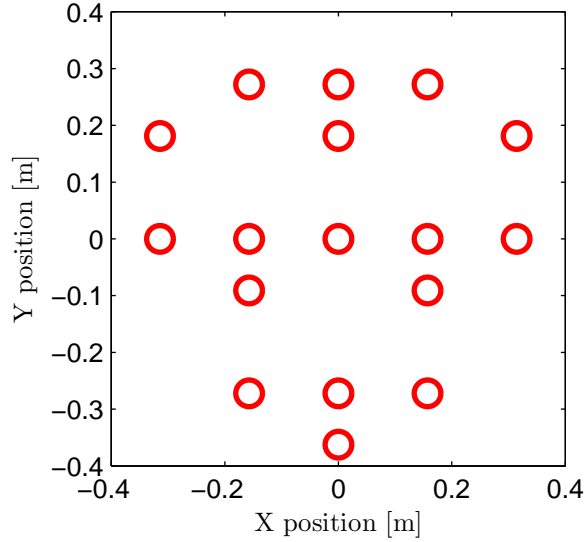
Figure 18. The union of the seven beam configurations used for multiple transmitters.

cate that correlation decreases as separation distance increases. This indicates that the model in Eqs. (127) and (128) produce a pessimistic estimate for multi-beam performance.

4.2.3 Simulation approach.

The simulation configuration used for the independent beam case was also used for the multiple, partially correlated beam case. To propagate the multi-beam configurations, a matrix of seventeen unique beam positions was created by determining the union of the seven beam configurations shown in Fig. 18. After propagating the beams and integrating them across the receiver, an $L \times M$ matrix of irradiances was created where L is the number of beam positions and M is the number of random realizations. An $M \times N$ evaluation matrix was created to convert the beam position irradiances to transmitter configuration irradiances where N is the number of transmitters.

One issue associated with the placement of multiple beams resulting from the

59

necessarily non-uniform separation distance for four or more beams is the variation in relative intensity over the receive aperture from each of the transmitters. When the beams are transmitted parallel to each other, beams placed further from the center clearly result in a smaller contribution to the aperture-averaged irradiance since the aperture intercepts the beam edge and not its center. As a result, fades from beams near the center could have a greater impact on the frequency of fades than those farther away. The model for partially correlated beams also assumes that each beam contributes to the mean irradiance equally. To compensate, the transmitted power for each beam was adjusted to ensure the mean power received from each beam is the same. Each transmitter's mean contribution to the integrated irradiance was determined by using Eq. (90) with the short term beam waist W_{ST} replaced by the long term beam waist W_{LT}. This resulted in an evaluation matrix of

$$
\begin{bmatrix}
1.0 & 0.0 & 0.0 & 0.0 & 0.17 & 0.0 & 0.12 \\
0.0 & 0.5 & 0.0 & 0.24 & 0.0 & 0.0 & 0.0 \\
0.0 & 0.5 & 0.0 & 0.24 & 0.0 & 0.0 & 0.0 \\
0.0 & 0.0 & 0.33 & 0.0 & 0.0 & 0.15 & 0.0 \\
0.0 & 0.0 & 0.33 & 0.0 & 0.0 & 0.15 & 0.0 \\
0.0 & 0.0 & 0.33 & 0.0 & 0.0 & 0.15 & 0.0 \\
0.0 & 0.0 & 0.0 & 0.26 & 0.0 & 0.0 & 0.0 \\
0.0 & 0.0 & 0.0 & 0.26 & 0.0 & 0.0 & 0.0 \\
0.0 & 0.0 & 0.0 & 0.0 & 0.0 & 0.18 & 0.0 \\
0.0 & 0.0 & 0.0 & 0.0 & 0.0 & 0.18 & 0.0 \\
0.0 & 0.0 & 0.0 & 0.0 & 0.0 & 0.18 & 0.0 \\
0.0 & 0.0 & 0.0 & 0.0 & 0.21 & 0.0 & 0.15 \\
0.0 & 0.0 & 0.0 & 0.0 & 0.21 & 0.0 & 0.15 \\
0.0 & 0.0 & 0.0 & 0.0 & 0.0 & 0.0 & 0.15 \\
0.0 & 0.0 & 0.0 & 0.0 & 0.0 & 0.0 & 0.15 \\
0.0 & 0.0 & 0.0 & 0.0 & 0.21 & 0.0 & 0.15 \\
0.0 & 0.0 & 0.0 & 0.0 & 0.21 & 0.0 & 0.15
\end{bmatrix} . \tag{135}
$$

Without compensating for the different beam powers the evaluation matrix would simple contain values where each column would only be populated by either a zero or $1/N$. This effectively would allow the contribution from beam to be equal for a given configuration.

4.2.4 Comparison of the results.

Using a combination of multiple beams and adjusting the power among the beams such that the mean power received from each is the same, a wave-optics simulation was

done showing the marginal improvement as the number of beams is increased. The CDF results are shown in Fig. 19. Additionally, the theoretical estimates determined using Eqs. (57), (127), and (133) were compared to the CDFs from simulation. The reduced fade probability is apparent as the number of transmitters is increased. For example, if the fade threshold is determined to be 0dBm, the probability of fade for one, two, four, and seven transmitters is 9.4×10^{-3}, 2.0×10^{-3}, 3.7×10^{-4}, and 1.5×10^{-4}, respectively. This shows that using more than four transmitters does little to improve the overall performance.

Fig. 19 shows that the model provides a good description of wave-optics results for up to four transmitters. As the number of transmitters increases past four, the model for the shaping parameters in Eqs. (127) and (128) appears to become less valid. The assumption of Gamma-Gamma statistics for off-center beams is likely failing again. Referring back to Fig. 13, one can see that as the number of transmitters increases, separations between the center of the beam configurations, where the receiver is located, and the most distant beams increase. This may account for the disagreement between the model and wave-optics simulations when the number of transmitters is greater than four.

Overall, the model provides a good tool for estimating the fade probability for a multiple-transmitter system. This would give engineers a method to investigate the design trade offs associated with the multi-beam systems.
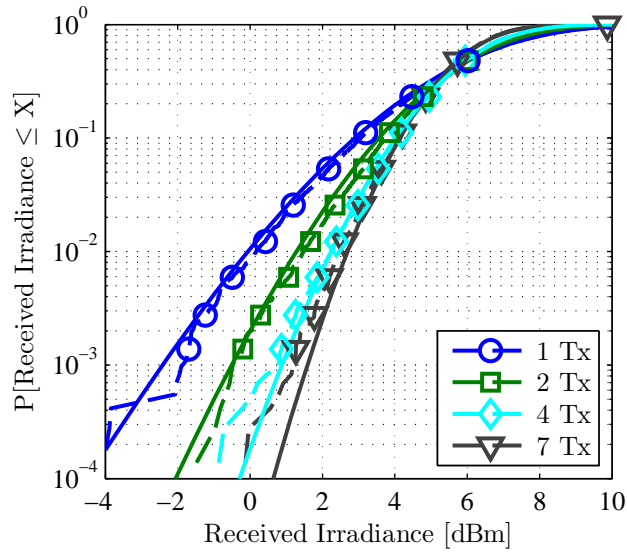
Figure 19. Analytical CDF, solid lines, and wave-optics results, dashed lines, plotted for one through seven spatially separated beams using the configurations shown in Fig. 13.

V. Communications System Performance

This chapter discusses the BER results for and ideal fixed threshold OOK and PPM. First, an analytical model for the BER for a multi-beam FSOC is developed. The next section provides a description of how the irradiance from the wave-optics simulation was used in combination with traditional BER models to calculate BER. Finally, a Monte Carlo analysis of the BER was performed using the irradiances from the wave-optics simulation. All three of these methods were compared with each other showing the significant increase in performance when multiple beams are used in combination with PPM over baseline method of a single beam with OOK.

The difference in performance between PPM and OOK highlights the difference between using a fixed threshold OOK modulation scheme which is highly sensitive to deep signal fades versus a scheme which is not significantly impacted by deep fades. In the case of OOK, a deep fade due to scintillation causes the received signal to drop below the threshold, resulting in every received bit being estimated as a signal low. Assuming the likelihood of a transmitted low or high signal is equal, this amounts to a 50% BER. Binary PPM places all of the energy either in the first half of the transmitted symbol or the second half. The receiver then subtracts the received energy for the first half of the symbol from the second half resulting in either a positive or negative value. With a threshold of zero, the negative values correspond with a signal low and positive values with a signal high. PPM does not require the constant detection and update of the threshold value, which draws irradiance from the communications detector [33]. Additionally, PPM always has either a rising or falling edge in the center of the pulse which could be used to aid in timing and synchronization of the demodulator [53]. The price of these benifits is a doubling of the bandwidth necessary to transmit and receive the PPM symbol compared to OOK.

5.1 Analytical model of BER

The analytical BER model starts with the calculation of BER for a binary signaling scheme. Using the detector model Eq. (1) and assuming that the channel gain is constant over the duration of a symbol, the BER for a given channel gain $P_B[h]$ can be determined via [52]

$$P_B[h] = P[s_0] P[H_1|s_0, h] + P[s_1] P[H_0|s_1, h], \tag{136}$$

where h represents the channel gain over the symbol duration and $s_{0,1}$ represents the two transmitted symbols for the binary signaling scheme. $P[s_{0,1}]$ is the probability that s_0 or s_1 was transmitted respectively, and $P[H_{0,1}|s_{0,1}, h]$ is the probability that the receiver hypothesized s_1 when s_0 was transmitted and vice versa for a given channel gain. The assumption that $h(t)$ is constant over the symbol duration requires that $T \ll 1/f_G$ where T is the symbol duration and f_G is the Greenwood frequency from Eq. (74). For all practical systems of interest this requirement is met [32,33,51]. It should also be noted that $h(t)$ is not a zero-mean process and is characterized using the same model developed in Chapter IV with a transmitted irradiance of 1W.

Using the model in Eq. (1) assuming AWGN, the probability of the two error conditions in Eq. (136) become

$$
\begin{aligned}
P[H_1|s_0, h] &= \int_{z_t}^{\infty} p(z|s_0, h) \, \mathrm{d}z \\
&= \int_{z_t}^{\infty} \frac{1}{\sigma_z \sqrt{2\pi}} \exp\left[-\frac{1}{2}\left(\frac{z - \mu_0}{\sigma_z}\right)^2\right] \mathrm{d}z \\
&= Q\left(\frac{z_t - \mu_0}{\sigma_z}\right) \tag{137} \\
P[H_0|s_1, h] &= Q\left(\frac{\mu_1 - z_t}{\sigma_z}\right), \tag{138}
\end{aligned}
$$

where z_t is the threshold from Eq. (8), $\mu_{0,1}$ is the test statistic mean values for s_0 and s_1 respectively, and σ_z is the standard deviation of the test statistic for s_0 and s_1 due to the AWGN. The operator $Q(\cdot)$ is the Q-function defined as

$$Q(x) = \frac{1}{\sqrt{2\pi}} \int\limits_{x}^{\infty} \exp\left(-\frac{u^2}{2}\right) \, du. \tag{139}$$

To calculate the total BER over all possible channel gains for a specific atmospheric path, the BER for each channel gain is combined with the probability of each channel gain value via

$$P_B = \int\limits_{0}^{\infty} P_B[h] \, p(h) \, dh, \tag{140}$$

where $p(h)$ is the PDF the channel gain. The PDF of the channel gain equivalent to the PDF of irradiance in Eq. (57) assuming a 1W transmitted power. The integral in Eq. (140) was evaluated numerically.

The difference between the performance of an ideal fixed-threshold OOK modulation scheme and a PPM modulation scheme simplifies to choosing the appropriate reference signal $s_{ref}(t)$. For OOK the reference signal is

$$s_{ref}(t) = u(t) \quad 0 > t \leq \frac{T}{2}, \tag{141}$$

while for PPM the reference signal is

$$s_{ref}(t) = -u(t) + 2u(t - T/2) \quad 0 > t \leq \frac{T}{2}, \tag{142}$$

where $u(t)$ is the unit step function. For the fixed threshold OOK case the threshold was based on Eq. (8). The expected test statistic value for receiving an on bit, μ_1 in Eq. (8), was calculated with a channel gain determined from Eq. (90) and replacing

the short-term beam waist with the long-term waist found in Eq. (91). The variance was calculated by summing the AWGN variance with the variance calculated from Eq. (59) using the shaping parameters from Eq. (127).

For PPM, since $\mu_0 = -\mu_1$ the threshold is zero. This means that regardless of the channel gain, the threshold is always optimal, resulting in a better BER compared to using fixed threshold OOK. The price for this improved performance is an increase in the bandwidth required by a factor of two.

5.2 BER with wave-optics

Calculation of the BER from the wave-optics results simply used the channel gains from each random realization of the atmosphere along the propagation path to calculate a BER based on random draws of the aperture averaged irradiace at the receiver. The BER for all the random realizations of the channel gains were averaged together to produce the overall BER for the propagation path. The ideal fixed threshold was determined by using the mean and variance of the test statistic from the simulation data and changed depending on the number of transmitters and the AWGN power. The PPM simulation used a threshold of zero. The simulation results from Section 4.2 were used to generate the channel gains by calculculating the ratio between the input irradiance and the integrated irradiance across the receiver.

5.3 Monte Carlo simulation of BER measurement

Additionally a Monte Carlo simulation was performed at each time-step to validate the analytical model. First, the Monte Carlo simulation generated a random bit pattern at an information bit rate of 1Gbps. The bit pattern was then modulated at a sampling rate of 200GHz using both OOK and PPM to create the symbols. Following the model in Eq. (1), the symbols were multiplied by the channel gain

from an instance of the wave-optics simulation and random draws AWGN noise were added. Then, the modeled detector output was multiplied by the reference signal and integrated over the symbol duration to obtain the test statistic shown in Eq. (2). The test statistic was then compared to the threshold to produce the bit estimates. The bit estimates were then compared to the original random bit pattern and differences were counted as bit errors. The process was repeated for each of $7,250$ random realizations of the wave-optics simulation. Prior to executing the simulation, the Monte Carlo simulation was validated using a fixed channel gain and only AWGN which produced results identical to the established models [52].

5.4   Comparison of results

A comparison of the results for all three methods are shown in Figs. 20 and 21. The calculated BER is shown as a function of E_b/N_0 where E_b is the transmitted signal energy per information bit and N_0 is the AWGN power over the receiver bandwidth. E_b/N_0 is related to SNR by

$$\frac{E_b}{N_0} = \frac{S}{N}\frac{W}{R} \tag{143}$$

where S is the signal power, N is the noise power, W is the bandwidth of the receiver, and R is the information bit rate. The results are limited to the aperture size used in the simulation, $D = 10$cm, but allows for a meaningful and fair comparison between the various transmitter configurations, since different transmitter configurations result in different mean received irradiance.

The use of additional transmitters clearly improves the BER seen in Figs. 20 and 21. However, the improvement is more dramatic for the fixed threshold OOK than the improvement for PPM. By way of comparison at a BER of 10^{-3}, the gain between one to two transmitters is 3.4dB for fixed threshold OOK and only 1.6dB for PPM. Similarly, the gain for going from two to four transmitters is 2.4dB for

68

Figure 20. BER for multiple beams using a fixed threshold OOK. The markers indicate results from the Monte Carlo simulation of the communications link. The dashed lines are the "analytical" results using the data from the wave-optics simulation. The solid line is the analytical result obtained from the newly derived model of the received intensity. Results are shown for one, two, four, and seven transmitters.

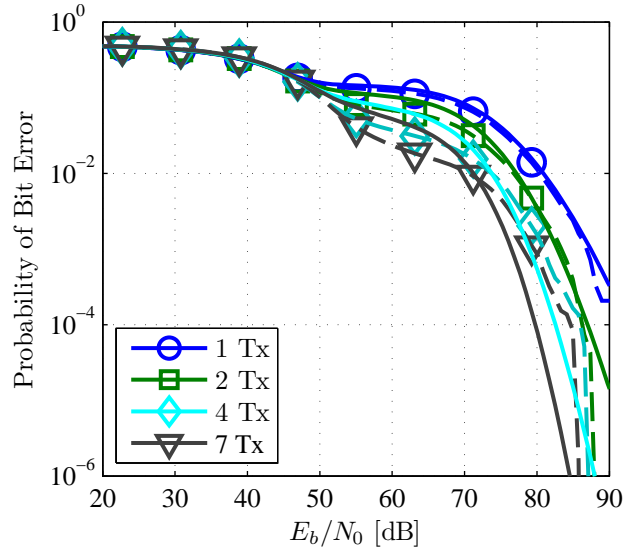**Figure 21.** BER for multiple beams using PPM. The markers indicate results from the Monte Carlo simulation of the communications link. The dashed lines are the "analytical" results using the data from the wave-optics simulation. The solid line is the analytical result obtained from the newly derived model of the received intensity. Results are shown for one, two, four, and seven transmitters.
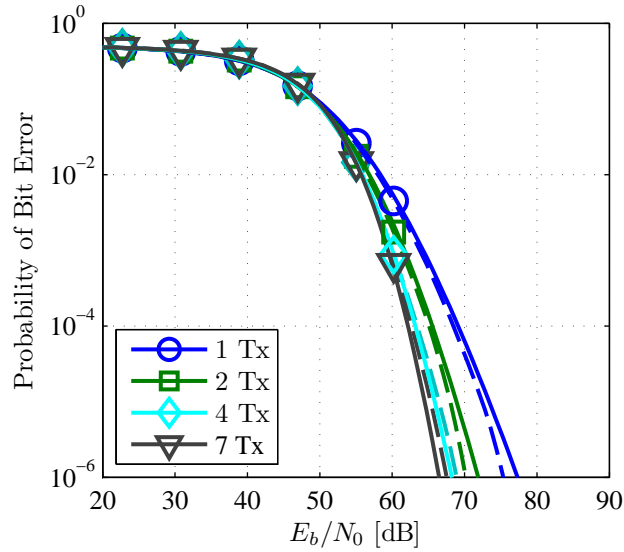
fixed threshold OOK and only 1.3dB for PPM. While gain is greater when fixed threshold OOK is used, the performance still does not surpass that of PPM, which at a BER of 10^{-3} PPM is 15.7dB better even when comparing seven transmitters using fixed threshold OOK against a single transmitter using PPM. Figure 20 also shows the more dramatic impact the modeling errors have in estimating the BER for fixed threshold OOK as the number of transmitters is increased. While the BER curve for one or two transmitters is modeled well, the assumptions used for determining the PDF for additional transmitters more dramatically impacts BER estimates. This is less evident for the PPM case shown in Fig. 21, where there is much better agreement between the model and simulation results.

Since PPM requires twice the bandwidth compared to OOK, a better comparison would be to use the extra bandwidth to implement FEC. An Extended Golay(24,12) algorithm was used in a Monte Carlo simulation to generate 24 channel bits for every 12 data bits. The encoded bits were then propagated through the channel at a rate of 2Gbps, twice the rate of the information bits. This results in the encoded OOK signal using the same bandwidth as PPM. After propagation through the channel and the addition of AWGN, the channel bit estimates were decoded to produce information bit estimates. Errors between the transmitted information bits and the information bit estimates were counted as errors. Fig. 22 shows the results of this simulation. For this FSOC scenario, where the bit errors for OOK are dominated by the channel fades, fixed threshold OOK with FEC shows little performance improvement over the baseline of fixed threshold OOK.
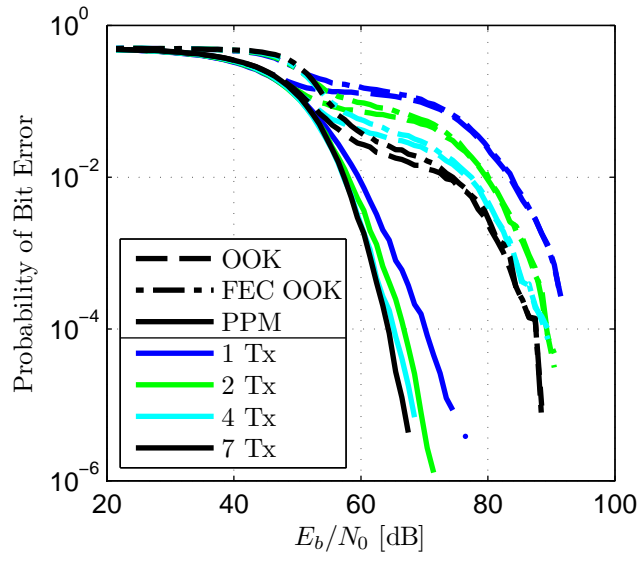
Figure 22. Simulation results for fixed threshold OOK and PPM compared with FEC OOK The results show that for this scenario, where the channel gain of the atmosphere dominates the bit errors, FEC does little to improve overall BER. Results are shown for one, two, four, and seven transmitters.

VI. Lab Experimentation

The results from a bench-top experiment using an atmospheric turbulence simulator (ATS) were compared with the model developed in Chapter IV. The in-lab experiment simulated a multi-beam communications system by transmitting a collimated laser through the turbulence simulator onto an imaging system. The imaging system is used to determine fade statistics, which were then compared to the previously developed model.

6.1 Lab description

To more accurately explore the complexities involved with an actual FSOC system, a bench-top laboratory demonstration was constructed taking advantage of existing equipment. The experiment validates the analytical model and wave-optics simulation by measuring the aperture-averaged irradiance using multiple transmitters. The overall system configuration is described below, followed by a more detailed description of ATS.

6.1.1 Configuration.

The basic layout of the experimental system is shown in Fig. 23. The laser diode, a Thorlabs LPS-PM1550-FC mounted to a Thorlabs TCLDM9 Temperature Controlled Laser Diode Mount shown in Fig. 24, emits a polarized 1550nm beam through a polarization-maintaining fiber. The emitted power level is tunable via a Thorlabs ITC8102 controller mounted in a PRO8000 chassis. The polarization-maintaining fiber connects to a Thorlabs F230FC-1550 fiber collimator resulting in a 0.9mm collimated beam. The beam then travels through the SAIC ATS described below. After exiting the ATS, the beam then relays off of a total of four relay mirrors used to
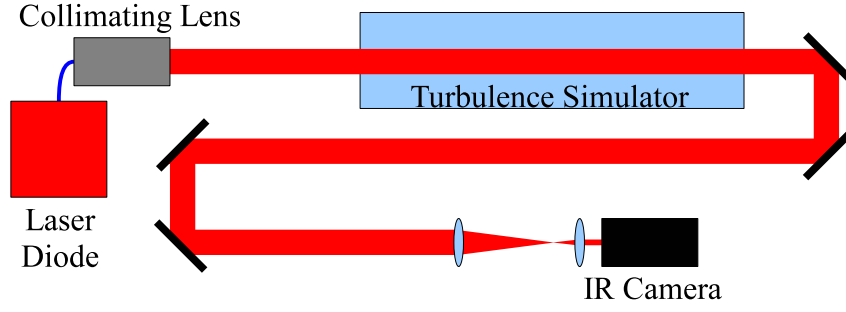
Figure 23. Lab experiment configuration.
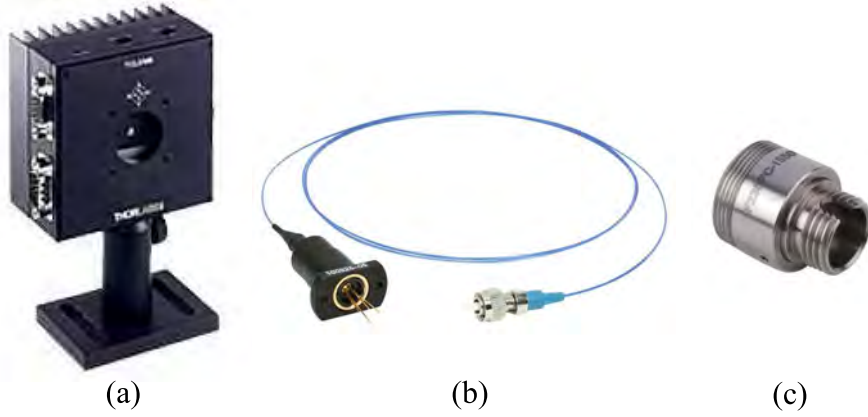
Figure 24. (a) **Thorlabs LPS-1550-FC Laser Diode,** (b) **Thorlabs TCLDM9 Temperature Controlled Laser Diode Mount,** (c) **Thorlabs F230FC-1550 1550nm Fiber Collimating Package.**

increase the distance between the ATS and the imaging system. The relay extends the total path length from a nominal 1m beyond the ATS, used for adaptive optics experiments, to 6.2m beyond the ATS.

The imaging system consists of two lenses configured as a 4-f system where a 1/4th magnification is imposed on the beam. The resulting image is received by a FLIR Alpha near infra-red (NIR) camera. The first lens has a focal length of 300mm, while the second lens has a focal length of 75mm. Both lenses are anti-reflection coated for the 1550nm beam. To find the camera image plane, a picture was placed on a filter mount and the camera position was adjusted until the picture came into focus.

Figure 25. Imaging system showing the 300mm lens and the 75mm lens followed by the FLIR Alpha NIR camera.

The camera was locked down and the picture removed, leaving the filter mount to mark the camera imaging plane position. The whole system could then be moved together to adjust the path length between the imaging system and the ATS without disturbing the imaging plane location relative to the camera.

Once the data are captured, a digital mask is applied to the saved images to simulate various aperture sizes. By moving the collimated beam, causing the beam to travel through a different portion of the turbulence generated by the ATS, the system can simulate multiple off-axis beams. The images are combined in post-processing to simulate multiple beams propagating at the same time.

6.1.2 Atmospheric turbulence simulator.

The turbulence simulator is an SAIC ATS, model 0003 shown in Fig. 26 [36, 44]. Using a combination of lenses and phase wheel modules, the ATS simulates atmospheric propagation for a variable range of turbulence parameters. By adjusting the phase wheel location, the density of the variations across the beam can be changed,
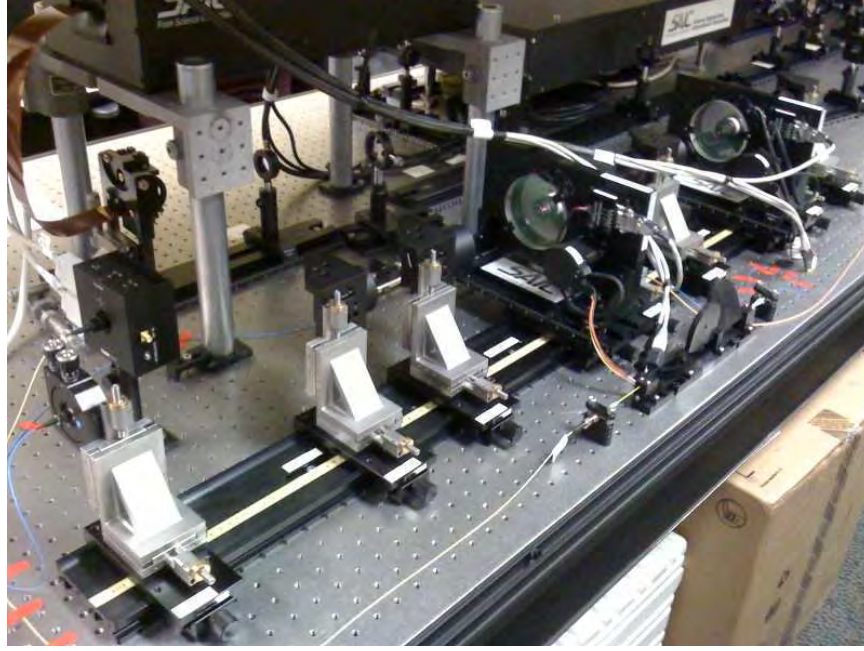
Figure 26. Atmospheric Turbulence Simulator.

since the phase wheel is in converging beam space. When this is combined with a variable rate in phase wheel rotation, the turbulence can be fine tuned to emulate a large parameter space of turbulent conditions. Additionally, the phase wheels themselves can be exchanged for an even greater degree of flexibility.

6.2 Methodology

The experiment was designed to replicate the scenario used in the wave-optics simulation. To accomplish this, several key parameters were used to scale the experiment to the simulation. However, the limitations of the lab setup required some deviations from the simulation. These key parameters, and the method used to calculate them from the experimental data, are described below. After that, the procedures used to capture the data are described.

Table 2. A comparison of the key parameters used in the simulation versus those used in the lab experiment. Those marked with a * are the non-dimensional scaling parameters.

Parameter	Simulation	Experiment
Transmitter Gaussian Beam Waist, W_0	5.0cm	0.45mm
Wavelength, λ	1550nm	1550nm
Path Length, L	100km	7.78m
Fresnel Ratio*, Λ_0	19.7	19.0
Rytov Variance*, σ_1^2	0.92	2.6
D/r_0*	0.32	0.32

6.2.1 Key parameters.

A comparison of parameters used in the simulation and those used in the lab experiment are shown in Table 2. The turbulence parameters σ_1^2 and D/r_0 are actual measured values for the experimental column. For the experiment and simulation to model the same scenario, it is required that the Fresnel ratio, Rytov variance, and D/r_0 are the same.

Determining the values for the experiment were straightforward for the wavelength and the transmitter beam waist. The wavelength of the Thorlabs LPS-PM1550-FC is 1550nm, and the output of the Thorlabs F230FC-1550 fiber collimator is fixed at a diameter of 0.9mm. However, due to the compressed design of the ATS, the path length is not just a simple measure of the distance from the output of the collimating lens to image plane of the imaging system. The method used for determining the path length takes advantage of the Gaussian beam propagation equations and solves for the propagation distance. Recalling Eqs. (23) and (26) the effective propagation distance L_e can be solved for using the measured propagated beam waist via

$$L_e = \frac{kW_0\sqrt{W^2 - W_0^2}}{2}. \tag{144}$$

The beam waist was determined by fitting a Gaussian profile to the received intensi-

ties. Once the effective propagation distance was determined, the Fresnel ratio was calculated. Adjustments were then made to the propagation path in an attempt to get the Fresnel ratio as close to the wave-optics simulation as possible.

Determining the turbulence parameters required measuring the resulting beam waists after propagating a beam through the turbulence. Calculating the atmospheric coherence length r_0 starts with the relationship between the long-term propagated beam waist W_{LT} and the short-term beam waist W_{ST} given as

$$W_{LT}^2 = W_{ST}^2 + \langle r_c^2 \rangle, \tag{145}$$

where $\langle r_c^2 \rangle$ is the second moment of the instantaneous center of the beam in the receiver plane [1]. The beam wander can be expressed in terms of r_0 via

$$\sqrt{\langle r_c^2 \rangle} = 0.69L \left(\frac{\lambda}{2W_0} \right) \left(\frac{2W_0}{r_0} \right)^{5/6}. \tag{146}$$

Using the effective propagation distance in place of L and solving for the experimental atmospheric coherence length $r_{0,e}$ yields

$$r_{0,e} = 2W_0 \left(\frac{\sqrt{W_{LT}^2 - W_{ST}^2}}{0.69L_e} \frac{2W_0}{\lambda} \right)^{-6/5}. \tag{147}$$

Since the experimental aperture was implemented digitally using a mask, the value for experimental D/r_0 was made to match the simulation exactly by making the experimental aperture size

$$D_e = r_{0,e} \frac{D}{r_0}. \tag{148}$$

The other turbulence parameter used to describe the experimental configuration is the plane-wave Rytov variance σ_1^2 defined in Eq. (55). Using Eq. (91) and assuming the transmitter is fixed and assumed to have no mechanically induced jitter, the

effective long-term beam waist can be calculated. Then solving for σ_1^2 yields

$$\sigma_1^2 = \left[\frac{0.307kW^2}{L_e}\left(\frac{W_{LT}^2}{W^2}\right)\right]^{5/6},\tag{149}$$

where W is the vacuum-propagated beam waist given by Eq. (26).

6.2.2 Experimental procedure.

The execution of the experiment consisted of the initial configuration, the data collection, and analyzing the data. The initial configuration consisted of aligning the beam and determining the effective propagation distance. The Thorlabs F230FC-1550 fiber collimator was placed in a Thorlabs K6X six-axis kinematic optic mount. The K6X was mounted on an elevation stage, which was then mounted on top of two translation stages allowing for a three-dimensional translation adjustment. The K6X allowed for small translations, but not large enough for the experiment. Once the transmitter was mounted and aligned, the measurement of effective propagation distance was made by capturing vacuum propagation images and using Eq. (144). Adjustments were then made to the location of the imaging system until the effective propagation distance was 8.1m, the distance needed to produce the same Fresnel ratio as the wave-optics simulation. However, the technique used to measure the propagation distance appeared to be very sensitive and only repeatable to about 95% accuracy. The value shown in Table 2 was the measured value obtained during the data collection.

Once the initial configuration was complete, the data taking process began. To take advantage of the same routines used to analyze the wave-optics simulation data, the same seventeen beam locations were used in the experiment. The beam separation used was $2\rho_c$, the same as the simulation. This resulted in an experimental distance of 1.4mm which, when considering the factor of four demagnification, translated into
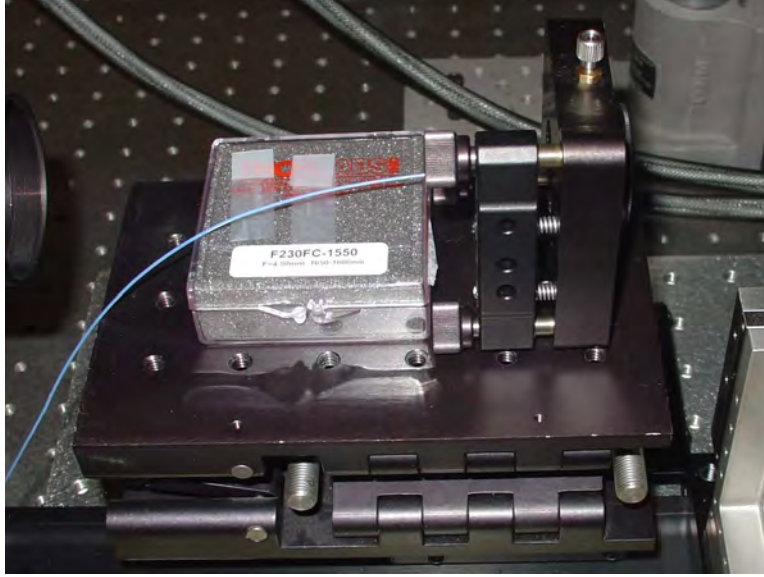
Figure 27. The mount used for the transmitted beam consisting of an elevation stage on top of two translation stages. The configuration allowed for translation adjustments in three dimensions and tip-tilt adjustments in two dimensions.

23.6 pixels. A table was then created, reproduced in Table 3 of the positions needed to capture all seventeen locations. Although the mount was very stable once moved, moving the beam in a repeatable manner proved to be very difficult. Eventually a technique where every movement of the beam was made such that the last turn of the knobs were always in the same direction. Although the angle of the mount would change when the knobs were turned, this technique helped to keep the final angle the same after each movement. The beam position was verified by moving the phase wheels of the ATS in their vacuum-propagation position and observing the centroid shown on the camera interface. Once the beam position was verified, the phase wheels were put back into their turbulence position. To collect the data, one phase wheel was moved at 0.5RPM and the other phase wheel was moved at 5.0RPM. Camera images where saved over a period of 125s, ensuring that a full rotation of the slower phase wheel, and twenty rotations of the faster one, were captured. In addition to the seventeen beam positions, a vacuum-propagated beam was captured at the

79

Table 3. **Table showing the relative and absolute locations of the beam center at the receiver. The table assumes the detector is centered on pixel** $158, 125$**.**

Position	Relative		Absolute	
	X	Y	X	Y
1	0.0	0.0	158.0	125.0
2	−11.8	0.0	146.2	125.0
3	11.8	0.0	169.8	125.0
4	00.0	13.6	158.0	138.6
5	−11.8	−6.8	146.2	118.2
6	11.8	−6.8	169.8	118.2
7	0.0	20.4	158.0	145.4
8	0.0	−20.4	158.0	104.6
9	−23.6	13.6	134.4	138.6
10	23.6	13.6	181.6	138.6
11	0.0	−27.2	158.0	97.8
12	−11.8	20.4	146.2	145.4
13	11.8	20.4	169.8	145.4
14	−23.6	0.0	134.4	125.0
15	23.6	0.0	181.6	125.0
16	−11.8	−20.4	146.2	104.6
17	11.8	−20.4	169.8	104.6

center beam position as well as a background image with the laser off. The averaged background image was subtracted from each of the beam positions, including the vacuum-propagation, prior to analyzing the data.

The data were analyzed in the same manner as the wave-optics simulation data. After determining the proper receiver diameter to match the simulation's D/r_0, a mask was applied to the images. The irradiance for each frame was calculated by spatially integrating the pixel intensities across the masked images. This process resulted in an irradiance matrix, which was then multiplied by the evaluation matrix in Eq. (135) to produce the irradiances for one to seven beams.
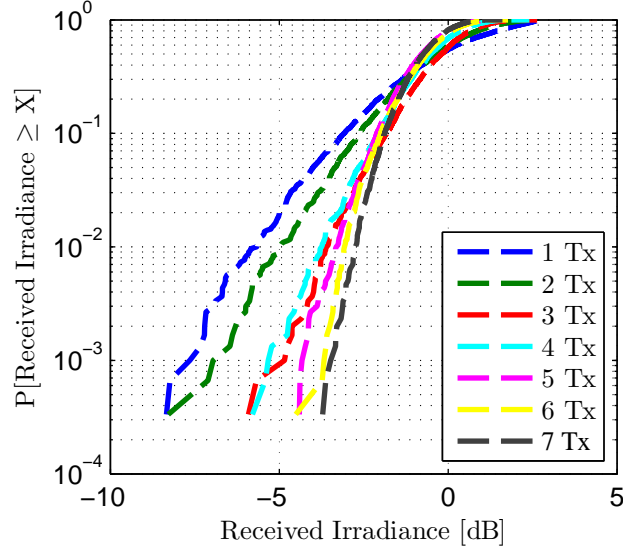
Figure 28. CDF of integrated irradiances for one to seven beams. Power is shown in dB's below the mean irradiance for a single beam.

6.3 Results

The results of the experiment for all seven configurations are shown in Fig. 28. The results are shown as a CDF normalized to the mean irradiance for a single beam. By normalizing in this way, the shifts in the CDF due to changes in the mean irradiance from the different beam configurations is preserved.

Figure 29 shows a comparison of the multi-beam model with the experimental data. An effective C_n^2 value was originally determined by calculating it from the atmospheric coherence length and the Rytov variance via Eqs. (43) and (55), respectively. The effective constant C_n^2 calculated from the atmospheric length was $6.8 \times 10^{-11} \mathrm{m}^{-2/3}$ while the value calculated from the Rytov variance was $9.8 \times 10^{-10} \mathrm{m}^{-2/3}$. However, the value determined to fit the single beam CDF best was $C_n^2 = 9.0 \times 10^{-11} \mathrm{m}^{-2/3}$. Both methods of estimating the turbulence are very sensitive to the estimate of the effective beam waist and the initial collimated beam waist. However, by using the single beam CDF to estimate the value of C_n^2 a good comparison can be made for the
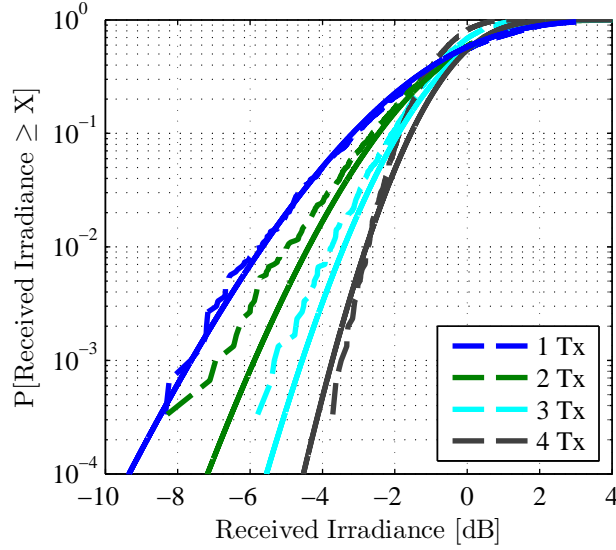
Figure 29. CDF of integrated irradiances for one, two, four and seven beams compared to model. Power is shown in dB's below the mean irradiance for a single beam.

multiple-beam cases.

6.4 Discussion

The model produces a reasonable prediction of the experimental results. Differences can partly be attributed to some of the unavoidable inconsistencies in the lab setup. Particularly, the method for positioning the beams may induce some pointing error resulting in the beams not traveling in parallel. Additionally, due to the nature of the stepper motors used on the phase wheels, the slow rotation of the first wheel caused a small amount of jitter in wheel's rotational rate. Finally, the camera frame rate was inconsistent due to the lack of an external trigger. This variation in the frame rate would cause the post-processed integrated irradiances to not properly average out the turbulence.

The model also contains some assumptions that are not present in the experiment or the simulation. The model essentially assumes that each transmitter is the same radial distance from the receiver, which for more than three transmitters is not

true. It does this by weighting their contribution to the new shaping parameters in Eqs. (127) and (128) equally. The wave-optics simulation violates this assumption in the same way, and experienced a similar disagreement with the model as the number of transmitters increased.

In summary, the performance of the new model has been assessed by comparing it with results from a wave-optics simulation and a lab experiment. While some of the assumptions used by the model are not valid in real world scenarios, the model still provides a useful tool for predicting the performance of a multi-beam FSOC system in turbulence. Additional testing of the model would be beneficial, particularly in a larger field experiment which would provide better scaling. A field experiment would also be able to use multiple transmitters at the same time, which would fix the alignment issues associated with moving a single beam to the different beam locations.

VII. Conclusion

This chapter discusses the final research conclusions. It includes some of the challenges that were overcome, the key research results and contributions, and some recommendations for future work.

7.1 Challenges overcome

The first challenge involved defining the problem to be researched and scoping the problem in such a way that the research would be completed in the time available. Building on previous free space optical communication (FSOC) work on from recent years, some fruitful research areas were found where overall performance improvements could be achieved. Previous multi-beam work was limited to using two transmitters, with the use of a larger number of transmitters and their configuration remaining uninvestigated.

The next challenge resulted from the lack of a verified probability distribution function (PDF) model for the irradiance resulting from multiple Gaussian beams. Fortunately, the development for the sum of independent Gamma-Gamma random variables was accomplished by Chatzidiamantis [8] shortly after this research began. By applying the foundations of single-beam irradiance PDFs from Andrews and Phillips [1, 2] and assuming the beams were independent, the combination provided a bounding solution. The resulting model was verified with wave-optics simulations in the course of this research. This model provided the basic framework for partially correlated beams. The method of determining the correlation coefficient as a function of beam separation provided the necessary foundation to determine the partially correlated PDF. Finally, weighting the contribution of the averaging effect between the beams by a function of the correlation coefficient ultimately resulted in a new

model, developed under this research, for multiple, spatially separated beams.

Another challenge involved settling on a method for propagating multiple beams in a wave-optics simulation, and the beam configuration. The orientation for two or three beams is straightforward. However, the use of four or more beams required a method to ensure the necessary beam spacing was maintained while minimizing the physical footprint required to house all of the beams. By using a hexagonal grid structure, the effective footprint of any number of beams is minimized. The beam positions are also such that the beam configurations are centered on the receiver and preferably symmetrical. These constraints led to the configurations shown in Fig. 13. To reduce the computation time required, the union of beam positions among the seven different configurations was determined resulting in the beam positions shown in Fig. 18. This ultimately reduced the number of individual beam propagations from 28 to 17 reducing computation time by 40%.

The last big challenge was determining methodology for propagating multiple beams in the lab experiment. The close beam spacing in the scaled experiment prevented them from simply being placed next to each other on a mount. Initially, a transmitter configuration was developed where up to four beams could be propagated simultaneously. However, maintaining beam alignment and spacing proved to be extremely difficult. This resulted in using a single beam which was iteratively moved to the different beam positions, similar to what was done in the wave-optics simulations. The initial mount did not provide the accuracy needed and was too limited in translation distance. Placing the mount on translation and elevation stages solved this problem, but introduced additional pointing errors that required some attention to ensure the error could be minimized and the beam positions were repeatable. Better fiber launch mounts may have eliminated some of the alignment problems, but such systems were well outside the available budget.

85

7.2 Key research results

This section summarizes the key results and contributions of this research.

7.2.1 Analytical PDF for multiple beams.

This work provides the first development of an analytical PDF model for a multi-beam FSOC system. The initial model assumes the beams are completely independent, providing a best-case scenario that bounds the performance of a multi-beam system. Building on previous work [31–33, 51], the necessary beam separation was then determined. This enabled development of a PDF model for multiple, spatially separated beams. Ultimately, this provides an engineering tool for performing design trade-offs between the number of beams used and other FSOC performance parameters.

7.2.2 Improved FSOC performance with PPM.

This work demonstrated FSOC BER improvement using pulse position modulation (PPM) for FSOC when experiencing scintillation. The obvious performance improvement is seen in Figs. 20 and 21 which demonstrate the utility of using PPM. Previous techniques using adaptive thresholding [33] with on/off keying (OOK) showed some improved performance. However, PPM inherently provides results that are consistent with what would be achieved using OOK with instantaneous, perfect adaptive thresholding. The cost of this improvement is a drop in bandwidth efficiency by a factor of two. Additionally, by combining multiple beams with PPM, significant BER performance gains can be achieved. This integration addresses the two aspects of scintillation in FSOC, including reducing the probability of fades and mitigating the impact of fades on overall BER.

7.2.3 Verification with experimental results.

This work provides experimental validation of a multi-beam model for FSOC applications. Previous work predominantly relied on on wave-optics simulations to verify multiple beam propagation effects [31–33, 51]. When used, experimentation with multiple beams was generally done for other applications [23] and not FSOC. Experimental validation in the context of FSOC systems further solidifies the improved irradiance statistics, namely the reduced scintillation as the number of transmitters is increased.

7.3 Recommendations for future work

During the course of this research several areas for future research were identified. These areas are summarized below.

7.3.1 Transmitter tracking and pointing.

Both the simulation and lab-based experimentation in this work was based on fixed transmitters and receivers, with transmitted beams being parallel to each other. The lab experiments highlighted the practical difficulty with aligning multiple beams such that they travel along parallel paths. In practice, a tracking system at the transmitter end would need to track the receiver to ensure proper beam pointing. This could aid in keeping the beams parallel, possibly by calculating the required offset needed for each beam. Another method would be to simply allow the beams to point to the receiver, resulting in converging rather than parallel beams. This would require a tracker for each transmitted beam. Regardless of the technique chosen, the model would need to be updated to account for not only the increased mean irradiance, but for the change in scintillation due to the pointing and tracking process itself. The tracker would effectively track, and therefore point, bright spots in the scintillation pattern which

might have the overall impact of reducing scintillation at the receiver [14].

7.3.2 Receiver optimization.

The receiver used for wave-optics simulation and lab-based experimentation used a direct-detection technique. While this allowed the research to concentrate on the irradiance statistics of multiple beams, it did not account for phase perturbations at the receiver. If the receiver were to couple the light onto a fiber, or focus the light to some other free-space detector, significant signal degradation would be introduced based on wavefront distortions.

In the case of multi-beam FSOC, the receiver design would also have to account for the received image of the multiple beams. If the receiver were able to resolve the different beams in the far-field, only light from the center beam may be coupled into the detector. Additionally, if the transmitters were designed to point towards the center of the receiver, each beam would reach the detector with different phase fronts. This will generally impact performance of a fiber coupler.

Bibliography

[1] Andrews, Larry C. and Ronald L. Phillips. *Laser Beam Propagation through Random Media, Second Edition*. SPIE Press, Bellingham, WA, 2nd edition, 2005.

[2] Andrews, Larry C., Ronald L. Phillips, and Cynthia Y. Hopen. *Laser Beam Scintillation with Applications*. SPIE Press, Bellingham, WA, 2nd edition, 2001.

[3] Anguita, Jaime A., Mark A. Neifeld, and Bane V. Vasic. "Multi-beam space-time coded systems for optical atmospheric channels". Volume 6304, 63041B+. SPIE, 2006.

[4] Arnon, Shlomi. "Use of Satellite Natural Vibrations to Improve Performance of Free-Space Satellite Laser Communication". *Appl. Opt.*, 37(21):5031–5036, July 1998.

[5] Berman, G. P., A. R. Bishop, B. M. Chernobrod, V. N. Gorshkov, D. C. Lizon, D. I. Moody, D. C. Nguyen, and S. V. Torous. "Reduction of laser intensity scintillations in turbulent atmospheres using time averaging of a partially coherent beam". *J. Phys. B*, 42(22):225403 (11pp), 2009.

[6] Burris, H. R., A. E. Reed, N. M. Namazi, M. J. Vilcheck, and M. Ferraro. "Use of Kalman filtering in data detection in optical communication systems with multiplicative noise". 2685–2688. May 2001.

[7] Chaman-Motlagh, A., V. Ahmadi, and Z. Ghassemlooy. "A modified model of the atmospheric effects on the performance of FSO links employing single and multiple receivers". *Journal of Modern Optics*, 57(1):37–42, 2010.

[8] Chatzidiamantis, Nestor D., George K. Karagiannidis, and Diomidis S. Michalopoulos. "On the Distribution of the Sum of Gamma-Gamma Variates and Application in MIMO Optical Wireless Systems". *2009 IEEE Global Telecommunications Conference*, 1–6. November 2009.

[9] Chen, Chunyi, Huamin Yang, Xin Feng, and Hui Wang. "Optimization criterion for initial coherence degree of lasers in free-space optical links through atmospheric turbulence". *Opt. Lett.*, 34(4):419–421, February 2009.

[10] Churnside, J. H. and R. J. Lataitis. "Wander of an optical beam in the turbulent atmosphere". 29:926–930, March 1990.

[11] Churnside, James H. "Aperture averaging of optical scintillations in the turbulent atmosphere". *Appl. Opt.*, 30(15):1982–1994, May 1991.

[12] Corrsin, Stanley. "On the Spectrum of Isotropic Temperature Fluctuations in an Isotropic Turbulence". *Journal of Applied Physics*, 22(4):469–473, 1951.

[13] Coy, Steve. "Choosing mesh spacings and mesh dimensions for wave optics simulation". Volume 5894, 589405+. SPIE, 2005.

[14] Crabtree, Peter N. *Performance-Metric Driven Atmospheric Compensation for Robust Free-Space Laser Communication*. Ph.D. thesis, Air Force Institute of Technology, 2003.

[15] Djordjevic, Ivan B. and Goran T. Djordjevic. "On the communication over strong atmospheric turbulence channels by adaptive modulation and coding". *Opt. Express*, 17(20):18250–18262, September 2009.

[16] Fried, David L. "Optical Resolution Through a Randomly Inhomogeneous Medium for Very Long and Very Short Exposures". *J. Opt. Soc. Am.*, 1372–1379, 1966.

[17] Fried, David L. "Aperture Averaging of Scintillation". *J. Opt. Soc. Am.*, 57(2):169–172, February 1967.

[18] Fried, David L. "Anisoplanatism in adaptive optics". *J. Opt. Soc. Am.*, 72:52+, January 1982.

[19] Gatt, Philip, Thomas P. Costello, Dean A. Heimmermann, Diana C. Castellanos, Arthur R. Weeks, and C. Martin Stickley. "Coherent optical array receivers for the mitigation of atmospheric turbulence and speckle effects". *Appl. Opt.*, 35(30):5999–6009, 1996.

[20] Goodman, Joseph W. *Introduction to Fourier optics*. The McGraw-Hill Companies, Inc., New York, 2nd edition, 1996.

[21] Gu, Yalong, Olga Korotkova, and Greg Gbur. "Scintillation of nonuniformly polarized beams in atmospheric turbulence". *Opt. Lett.*, 34(15):2261–2263, 2009.

[22] Haas, Shane M. *Capacity of and Coding for Multiple-Aperture, Wireless, Optical Communications*. Ph.D. thesis, Massachusetts Institute of Technology, 2003.

[23] Higgs, Charles, Herbert T. Barclay, Salvatore J. Cusumano, and Kenneth W. Billman. "Active tracking using multibeam illumination". Volume 3381, 160–167. SPIE, 1998.

[24] Huntington, Andrew, Madison Compton, Sam Coykendall, George Soli, and George M. Williams. "Linear-mode single-photon-sensitive avalanche photodiodes for GHz-rate near-infrared quantum communications". *2008 IEEE Military Communications Conference*, 1–6. November 2008.

[25] Ji, Xiaoling and Xiaoqing Li. "Directionality of Gaussian array beams propagating in atmospheric turbulence". *J. Opt. Soc. Am. A*, 26(2):236–243, February 2009.

[26] Lange, Robert, Berry Smutny, Bernhard Wandernoth, Reinhard Czichy, and Dirk Giggenbach. "142 km, 5.625 Gbps free-space optical link based on homodyne BPSK modulation". Volume 6105, 61050A+. SPIE, 2006.

[27] Lee, Shinhak, James W. Alexander, and Muthu Jeganathan. "Pointing and tracking subsystem design for optical communications link between the International Space Station and ground". Volume 3932, 150–157. SPIE, 2000.

[28] Li, Xiaoqing and Xiaoling Ji. "Angular spread and directionality of the Hermite-Gaussian array beam propagating through atmospheric turbulence". *Appl. Opt.*, 48(22):4338–4347, August 2009.

[29] Louthain, James A. *Atmospheric turbulence scintillation effects of wavefront tilt estimation.* Master's thesis, Air Force Institute of Technology, 1997.

[30] Louthain, James A. *Integrated Approach to Airborne Laser Communication.* Ph.D. thesis, Air Force Institute of Technology, 2009.

[31] Louthain, James A. and Jason D. Schmidt. "Anisoplanatism in airborne laser communication". *Opt. Express*, 16(14):10769–10785, July 2008.

[32] Louthain, James A. and Jason D. Schmidt. "Integrated approach to airborne laser communication". Volume 7108, 71080F+. SPIE, 2008.

[33] Louthain, James A. and Jason D. Schmidt. "Synergy of adaptive thresholds and multiple transmitters in free-space optical communication". *Opt. Express*, 18(9):8948–8962, April 2010.

[34] Lyke, Stephen D., David G. Voelz, and Michael C. Roggemann. "Probability density of aperture-averaged irradiance fluctuations for long range free space optical communication links". *Appl. Opt.*, 48(33):6511–6527, November 2009.

[35] Ma, Jing, Yijun Jiang, Siyuan Yu, Liying Tan, and Wenhe Du. "Packet error rate analysis of OOK, DPIM and PPM modulation schemes for ground-to-satellite optical communications". *Opt. Commun.*, 283(2):237–242, January 2010. ISSN 00304018.

[36] Mantravadi, Samuel V., Troy A. Rhoadarmer, and Robert S. Glas. "Simple laboratory system for generating well-controlled atmospheric-like turbulence". Volume 5553, 290–300. SPIE, 2004.

[37] Obukhov, A. M. "Structure of the temperature field in turbulent flow". *Izv. Akad. Nauk. SSSR*, 13(8):58–69. ISSN 0148-0227.

[38] Ohtsuki, T. "Turbo-coded atmospheric optical communication systems". *2002 IEEE International Conference on Communications. Conference Proceedings. ICC 2002 (Cat. No.02CH37333)*, 2938–2942. IEEE, 2002.

91

[39] Peleg, Avner and Jerome V. Moloney. "Scintillation index for two Gaussian laser beams with different wavelengths in weak atmospheric turbulence". *J. Opt. Soc. Am. A*, 23(12):3114–3122, December 2006.

[40] Polynkin, Pavel, Avner Peleg, Laura Klein, Troy Rhoadarmer, and Jerome Moloney. "Optimized multiemitter beams for free-space optical communications through turbulent atmosphere". *Opt. Lett.*, 32(8):885–887, April 2007.

[41] Popoola, W. O., Z. Ghassemlooy, C. G. Lee, and A. C. Boucouvalas. "Scintillation effect on intensity modulated laser communication systems-a laboratory demonstration". *Opt. Laser Technol.*, 42:682–692, June 2010.

[42] Razavi, M. and J. H. Shapiro. "Wireless optical communications via diversity reception and optical preamplification". *IEEE International Conference on Communications, 2003. ICC '03.*, 2262–2266. IEEE, 2003.

[43] Razavi, M. and J. H. Shapiro. "Wireless optical communications via diversity reception and optical preamplification". *IEEE Trans. Wireless Commun.*, 4(3):975–983, May 2005. ISSN 1536-1276.

[44] Rhoadarmer, Troy A. and Angel. "Low-Cost, Broadband Static Phase Plate for Generating Atmosphericlike Turbulence". *Appl. Opt.*, 40(18):2946–2955, June 2001.

[45] Ricklin, Jennifer C. and Frederic M. Davidson. "Atmospheric turbulence effects on a partially coherent Gaussian beam: implications for free-space laser communication". *J. Opt. Soc. Am. A*, 19(9):1794–1802, September 2002.

[46] Ricklin, Jennifer C. and Frederic M. Davidson. "Atmospheric optical communication with a Gaussian Schell beam". *J. Opt. Soc. Am. A*, 20(5):856–866, May 2003.

[47] Roggemann, Michael C. and Byron Welsh. *Imaging Through Turbulence*. CRC Press, Boca Raton, FL, 1996.

[48] Ryan, P. T., W. H. Lowrey, I. A. De La Rue, and R. Q. Fugate. "Scintillation characterization for multiple beams". Volume 3763, 210–217. SPIE, October 1999.

[49] Sasiela, Richard J. *Electromagnetic Wave Propagation in Turbulence: Evaluation and Application of Mellin Transforms*. SPIE Publications, 2nd edition, May 2007.

[50] Schmidt, Jason D. *Numerical Simulation of Optical Wave Propagation With Examples in MATLAB (Press Monograph)*. SPIE Press, pap/chrt edition, August 2010.

[51] Schmidt, Jason D. and James A. Louthain. "Integrated approach to free-space optical communication". Volume 7200, 72000I+. SPIE, 2009.

[52] Sklar, Bernard. *Digital Communications: Fundamentals and Applications (2nd Edition)*. Prentice Hall, 2 edition, January 2001.

[53] Tahir, N., N. Mohamad Saad, B. B. Samir, V. K. Jain, and S. A. Aljunid. "Binary pulse position modulation simulation system in free space optical communication systems". 1–4. June 2010.

[54] Tellez, Jason A. and Jason D. Schmidt. "Multi-beam transmitter geometries for free-space optical communications". Volume 7588, 758803+. SPIE, 2010.

[55] Tellez, Jason A. and Jason D. Schmidt. "Multibeam scintillation cumulative distribution function". *Opt. Lett.*, 36(2):286–288, January 2011.

[56] Tellez, Jason A. and Jason D. Schmidt. "Multiple transmitter performance with appropriate amplitude modulation for free-space optical communication". *Appl. Opt.*, 50(24):4737–4745, Aug 2011.

[57] Terry J. Brennan, Phillip H. Roberts and David C. Zimmerman. *WaveProp, A Wave Optics Simulation System*. the Optical Sciences Company, Anaheim, CA, 2008.

[58] Toyoshima, Morio, Takashi Jono, Keizo Nakagawa, and Akio Yamamoto. "Optimum divergence angle of a Gaussian beam wave in the presence of random jitter in free-space laser communication systems". *J. Opt. Soc. Am. A*, 19(3):567–571, March 2002.

[59] Trisno, S. and C. C. Davis. "Performance of free space optical communication systems using polarization shift keying modulation". Volume 6304. SPIE, September 2006.

[60] Tyson, Robert K. *Principles of Adaptive Optics, Second Edition*. Academic Press, 2nd edition, October 1997.

[61] Tyson, Robert K., Douglas E. Canning, and Jeffrey S. Tharp. "Measurement of the bit-error rate of an adaptive optics, free-space laser communications system, part 1: tip-tilt configuration, diagnostics, and closed-loop results". *Opt. Eng.*, 44(9):096002+, 2005.

[62] Tyson, Robert K., Jeffrey S. Tharp, and Douglas E. Canning. "Measurement of the bit-error rate of an adaptive optics, free-space laser communications system, part 2: multichannel configuration, aberration characterization, and closed-loop results". *Opt. Eng.*, 44(9):096003+, 2005.

[63] Verdeyen, Joseph T. *Laser Electronics*. Prentice Hall, New Jersey, 3rd edition, 1995.

[64] Wu, Hanling, Haixing Yan, and Xinyang Li. "Modal correction for fiber-coupling efficiency in free-space optical communication systems through atmospheric turbulence". *Optik*, September 2009. ISSN 00304026.

[65] Xiao, Xifeng and David Voelz. "On-axis probability density function and fade behavior of partially coherent beams propagating through turbulence". *Appl. Opt.*, 48:167–175, 2009.

[66] Yenice, Yusuf E. and Barry G. Evans. "Adaptive beam-size control for ground-to-satellite laser communications". Volume 3266, 221–230. SPIE, 1998.

[67] Yenice, Yusuf E. and Barry G. Evans. "Adaptive beam-size control scheme for ground-to-satellite optical communications". *Opt. Eng.*, 38(11):1889–1895, 1999.

[68] Yu, M., J. Li, and J. C. Ricklin. "Efficient forward error correction coding for free-space optical communications". Volume 5550, 344–353. SPIE, October 2004.

[69] Yuksel, Heba and Christopher C. Davis. "Aperture averaging analysis and aperture shape invariance of received scintillation in free-space optical communication links". Volume 6304, 63041E+. SPIE, 2006.

[70] Yuksel, Heba, Christopher C. Davis, and Linda Wasiczko. "Aperture Averaging Experiment for Optimizing Receiver Design and Analyzing Turbulence on Free Space Optical Communication Links". Technical Digest (CD), CTuG4+. OSA, May 2005.

[71] Yuksel, Heba, Stuart Milner, and Christopher Davis. "Aperture averaging for optimizing receiver design and system performance on free-space optical communication links". *J. Opt. Netw.*, 4(8):462–475, August 2005.

[72] Zhang, Yixin, Tuo Zhu, and Chunkan Tao. "Aperture-averaging effects for weak to strong scintillations in turbulent atmosphere". *Chin. Opt. Lett.*, 2(7):373–375, July 2004.

[73] Zhao, Xinhui, Yong Yao, Yunxu Sun, and Chao Liu. "Circle Polarization Shift Keying With Direct Detection for Free-Space Optical Communication". *J. Opt. Commun. Netw.*, 1(4):307–312, September 2009.

[74] Zhao, Zhijun, Rui Liao, Stephen D. Lyke, and Michael C. Roggemann. "Direct detection free-space optical communications through atmospheric turbulence". *2010 IEEE Aerospace Conference*, 1–9. IEEE, March 2010.

[75] Zhao, Zhijun, Rui Liao, Stephen D. Lyke, and Michael C. Roggemann. "Reed-Solomon coding for free-space optical communications through turbulent atmosphere". *2010 IEEE Aerospace Conference*, 1–12. IEEE, March 2010.

[76] Zhu, Xiaoming and J. M. Kahn. "Performance bounds for coded free-space optical communications through atmospheric turbulence channels". *IEEE Trans. Commun.*, 51(8):1233–1239, August 2003. ISSN 0090-6778.

REPORT DOCUMENTATION PAGE

The public reporting burden for this collection of information is estimated to average 1 hour per response, including the time for reviewing instructions, searching existing data sources, gathering and maintaining the data needed, and completing and reviewing the collection of information. Send comments regarding this burden estimate or any other aspect of this collection of information, including suggestions for reducing the burden, to Department of Defense, Washington Headquarters Services, Directorate for Information Operations and Reports (0704-0188), 1215 Jefferson Davis Highway, Suite 1204, Arlington, VA 22202-4302. Respondents should be aware that notwithstanding any other provision of law, no person shall be subject to any penalty for failing to comply with a collection of information if it does not display a currently valid OMB control number.
PLEASE DO NOT RETURN YOUR FORM TO THE ABOVE ADDRESS.

1. REPORT DATE (DD-MM-YYYY)	2. REPORT TYPE	3. DATES COVERED (From - To)
15 Sep 2011	Dissertation	12 May 2008 - 15 Sep 2011

4. TITLE AND SUBTITLE

Integrated Approach to Free Space Optical Communications in Strong Turbulence

5a. CONTRACT NUMBER

5b. GRANT NUMBER

F1ATA0035J001

5c. PROGRAM ELEMENT NUMBER

6. AUTHOR(S)

Tellez, Jason A. LtCol

5d. PROJECT NUMBER

11G292N

5e. TASK NUMBER

5f. WORK UNIT NUMBER

7. PERFORMING ORGANIZATION NAME(S) AND ADDRESS(ES)

Air Force Institute of Technology
Graduate School of Engineering and Management (AFIT/EN)
2950 Hobson Way
Wright-Patterson AFB OH 45433-7765

8. PERFORMING ORGANIZATION REPORT NUMBER

AFIT/DEE/ENG/11-11

9. SPONSORING/MONITORING AGENCY NAME(S) AND ADDRESS(ES)

Air Force Office of Scientific Research
Kent Miller
3875 Randolph St., Suite 3112
Arlington, VA 22203
(703)696-8573, kent.miller@afosr.af.mil

10. SPONSOR/MONITOR'S ACRONYM(S)

AFOSR/NE

11. SPONSOR/MONITOR'S REPORT NUMBER(S)

12. DISTRIBUTION/AVAILABILITY STATEMENT

Approval for public release; distribution is unlimited.

13. SUPPLEMENTARY NOTES

14. ABSTRACT

The propagation of a free space optical communication signal through atmospheric turbulence experiences random fluctuations in intensity, including signal fades which negatively impact the communications link performance. This research develops an analytical probability density function (PDF) to model the best case scenario of using multiple independent beams to reduce the intensity fluctuations. The PDF was further developed to account for partially correlated beams, such as would be experienced by beams having finite separation. The PDF was validated with results obtained from digital simulations as well as lab experiments. The research showed that as the number of transmitted beams increases the probability of fade decreases. While fade probability is reduced by adding more beams, using more than four transmitters does little to improve the overall performance. Additionally, the use of pulse position modulation (PPM) provided significant improvement over traditional fixed threshold on/off keying with the impact of signal fading reduced. Combining PPM with multiple transmitters produced the best overall bit error rate results.

15. SUBJECT TERMS

free-space optical communication, atmospheric turbulence, spatial diversity, multiple-transmitters, optical modulation

16. SECURITY CLASSIFICATION OF:			17. LIMITATION OF ABSTRACT	18. NUMBER OF PAGES	19a. NAME OF RESPONSIBLE PERSON
a. REPORT	b. ABSTRACT	c. THIS PAGE			Maj. Jason D. Schmidt
U	U	U	UU	108	19b. TELEPHONE NUMBER (Include area code) (937) 255-3636 x7224 jason.schmidt@afit.edu